Key Points:

- Oceanic crust in the north-eastern Lau Basin formed at the now reorganized FRSC-MTJ system
- The position and the opening mechanisms of back-arc basin spreading center's change more dynamically at mid-ocean ridges
- Different opening mechanisms at the southern Mangatolu Triple Junction and northern Fonualei Rift Spreading Center despite their proximity

Correspondence to:

A. Jegen,
ajegen@geomar.de

Extension Dynamics of the Northern Fonualei Rift and Spreading Center and the Southern Mangatolu Triple Junction in the Lau Basin at 16°S

A. Jegen[1] , A. Dannowski[1] , M. Schnabel[2] , U. Barckhausen[2] , P. A. Brandl[1] , M. Riedel[1] , A. Beniest[3] , I. Heyde[2] , M. D. Hannington[1,4], A. Sandhu[1], R. Werner[1,†], and H. Kopp[1,5]

[1]GEOMAR, Helmholtz Centre for Ocean Research, Kiel, Germany, [2]BGR, Federal Institute for Geosciences and Natural Resources, Hanover, Germany, [3]Vrije Universiteit Amsterdam, Amsterdam, The Netherlands, [4]Department of Earth and Environmental Sciences, University of Ottawa, Ottawa, ON, Canada, [5]Department of Geosciences, CAU, Kiel University, Kiel, Germany

Abstract Due to the complexity of 2D magnetic anomaly maps north of 18°S and the sparsity of seismic data, the tectonic evolution of the northern Lau Basin has not yet been unraveled. We use a multi-method approach to reconstruct the formation of the basin at ~16°S by compiling seismic, magnetic, gravimetric and geochemical data along a 185 km-long crustal transect. We identified a crustal zonation which preserves the level of subduction input at the time of the crust's formation. Paired with the seafloor magnetization, the crustal zonation enabled us to qualitatively approximate the dynamic spreading history of the region. Further assessment of the recent tectonic activity and the degree of tectonic overprinting visible in the crust both suggest a complex tectonic history including a dynamically moving spreading center and the reorganizing of the local magma supply. Comparing the compiled data sets has revealed substantial differences in the opening mechanisms of the two arms of the Overlapping Spreading Center (OSC) that is made up by the northernmost tip of the Fonualei Rift and Spreading Center in the east and the southernmost segment of the Mangatolu Triple Junction in the west. The observed transition from a predominantly tectonic opening mechanism at the eastern OSC arm to a magmatic opening mechanism at the western OSC arm coincides with an equally sharp transition from and strongly subduction influenced crust to a crust with virtually no subduction input. The degree of subduction input alters the geochemical composition, as well as the lithospheric stress response.

Plain Language Summary The opening of back-arc basins is often described as analogy to mid-ocean ridge spreading, where the only difference is the force driving the extension. However, the northern Lau Basin is a prime example for the shortcomings of this analogy since its crust preserves an image of its complex tectonic history. The complexity results from the short-lived nature of zones of active rifting and spreading in the northern Lau Basin, which is very different from the temporally and spatially steady nature of spreading centers at mid-ocean ridges. The analysis of different methods (wide angle seismic data using ocean bottom seismometers, multi-channel seismic, magnetic, gravity, and geochemical data) has led us to conclude that the Lau Basin's crust at 15°30′–17°20′S was formed by a dynamically changing, both in regard of magma composition and position, extensional system that consists of the Fonualei Rift and Spreading Center and the Mangatolu Triple Junction. Nevertheless, the crustal zonation, formed by the varying subduction influence during its formation, is still preserved and affects the stress response of the crust and thus the present-day tectonic behavior.

1. Introduction

The Lau Basin was the first back-arc basin (BAB) ever to be recognized as such (Karig, 1970) and has therefore shaped our understanding of BAB dynamics and evolution. The formation of a BAB starts with the rifting of the adjacent volcanic arc until a point of crustal failure is reached, after which upwelling material can break through the crust, creating new, oceanic crust, hence initiating seafloor spreading (J. W. Hawkins, 1976; Karig, 1970; Molnar & Atwater, 1978; Taylor & Karner, 1983). The imposed extensional forces are typically generated by slab rollback or slab anchoring (Heuret & Lallemand, 2005) and are known to manifest themselves through rifting of the volcanic arc because the arc is the lithospheric weak point of the subduction setting (Molnar & Atwater, 1978).

Once seafloor spreading is initiated, it will then continue until extensional forces cease (Chase, 1978; Scholz & Campos, 1995).

In the northern Lau Basin, the extension is dispersed and accommodated by several individual zones of active rifting and spreading (Bird, 2003). Two of these extensional zones are the Fonualei Rift and Spreading Center (FRSC) and the southern branch of the Mangatolu Triple Junction (MTJ-S2), which overlap at about 16°10′S (Figure 1). Axial segmentation classification, as is typically applied at mid-ocean ridges (MacDonald et al., 1991), has led to the identification of an overlapping spreading center (OSC) connecting the two second order ridge segments, the MTJ-S2 and FRSC1 (Sleeper et al., 2016). In the course of our study, the back-arc crust adjacent to the OSC is assigned to distinct geological domains, the properties of which are then used to reconstruct a model of the crustal evolution. Additionally, the dominant opening mechanism of both OSC arms is determined. For this, we analyzed a variety of data acquired along a 185-km-long transect during the expedition SO267 (Hannington et al., 2019), which includes ocean bottom seismometer (OBS) data, multi-channel seismic (MCS) data, sub-bottom profiler data, magnetic data, gravimetric data and geochemical data from dredge samples (Figure 1).
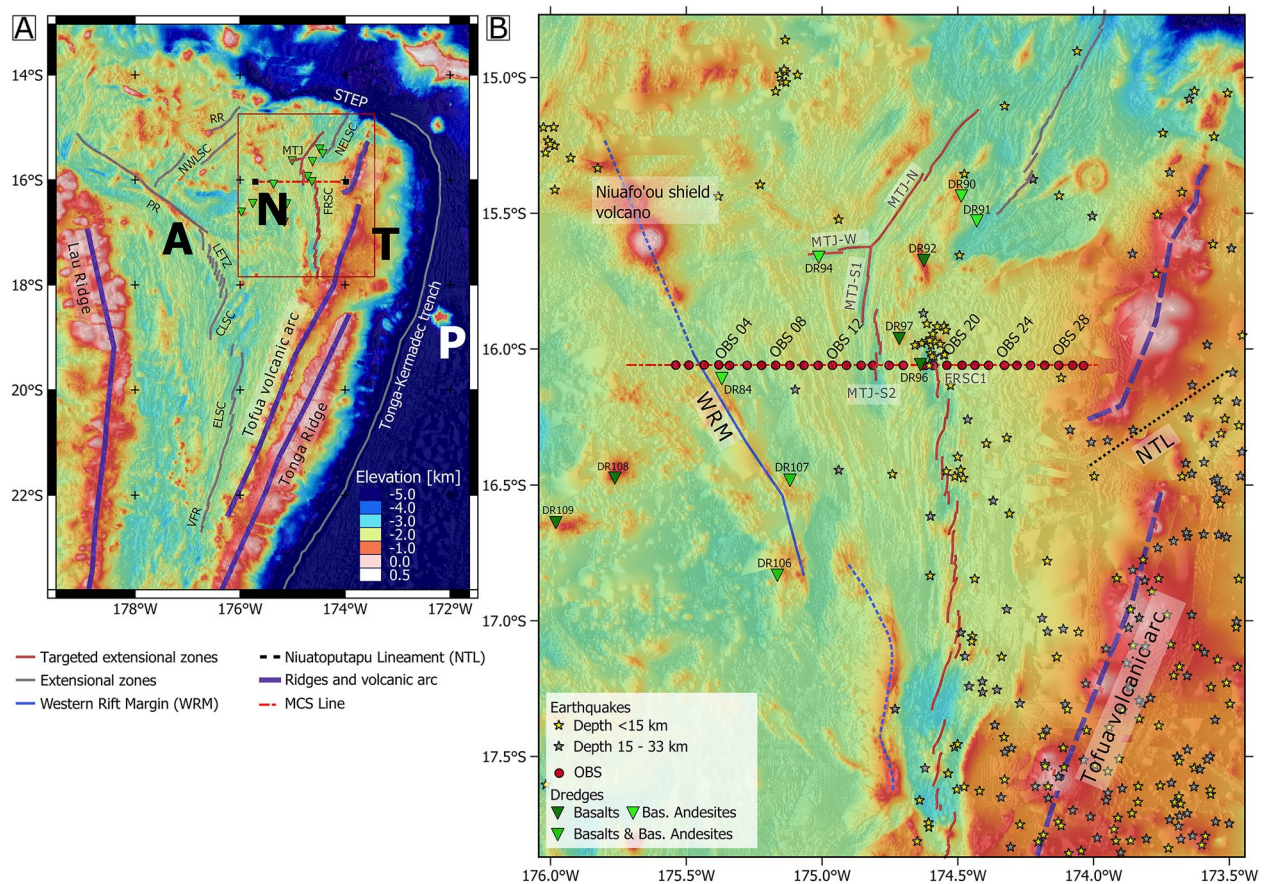
Figure 1. Bathymetric map (data compilation as seen in Stewart et al., 2022) showing the general region (a) as well as a detailed map of the study area in (b). Superimposed are the course of prominent tectonic features, shallow seismicity data from Conder and Wiens (2011) (stars), the course of the multi-channel seismic profile (red, dashed line), the positions of the deployed ocean bottom seismometer (red dots) and the dredge locations of the SO267 expedition (green triangles). The shade of green, chosen for the triangles, reflects how mafic the recovered samples are: Light green fore basaltic andesites, medium shade of green for basaltic andesites and basalts and dark green for basalts. Both the Mangatolu Triple Junction (MTJ) and the Fonualei Rift and Spreading Center (FRSC) are marked by red solid lines in both subplots and their most referenced segments (MTJ-S1, MTJ-S2, and FRSC1) are marked individually with dark gray labels in subplot (b). Other tectonic features such as the Tonga-Kermadec trench, the Tonga Ridge, the Tofua volcanic arc with its Niuatoputapu Lineament (NTL), the Lau Ridge, the Subduction-Transform-Edge-Propagator (STEP), the Niuafo'ou shield volcano, the North-East Lau Spreading Center (NELSC), Rochambeau Bank and Rifts (RR), Northwest Lau Spreading Center (NWLSC), Peggy Ridge (PR), Lau Extensional Transform Zone (LETZ), Central Lau Spreading Center (CLSC), Eastern Lau Spreading Center (ELSC) and the Valu Fa Ridge (VFR) are also marked. Additionally, plates and microplates are marked by bold letters in subplot (a): Australian Plate (a), Niuafo'ou microplate (N), Tonga Plate (T), Pacific Plate (P) after Sleeper and Martinez (2016). The same bathymetry color scale is used in both subplots.

2. Geological Background

2.1. Evolution and Prominent Structures of the Lau Basin

The Lau Basin is an actively forming BAB west of the Tofua volcanic arc front, which is the volcanic arc that is associated with the Tonga-Kermadec trench, where the Pacific Plate is subducted under the Australian Plate (Figure 1). The formation of the Lau Basin was induced by the rollback of the Pacific slab, which initiated rifting of the former Lau Tonga paleo-arc at approximately 6 Ma (Karig, 1970; Ruellan et al., 2003; Stewart et al., 2022). Rifting commenced in the northern Lau Basin and propagated southward following the asymmetric rollback of the Pacific Plate (Parson et al., 1994; Ruellan et al., 2003; Taylor et al., 1996). Continued extension created the current configuration of the western, remnant Lau Ridge and the eastern Tonga Ridge (Taylor et al., 1996; Wiedicke & Collier, 1993). Following the southwards propagating rifts, rifting transitioned to seafloor spreading starting in the north and progressing southwards (Parson et al., 1994; Ruellan et al., 2003; Taylor et al., 1996). Today, the basin has a characteristic triangular shape with the lowest opening rates in the south, where the basin is the narrowest (~200 km) and the highest opening rates in the north where the basin reaches its maximum width of ~500 km (Anderson et al., 2021; Bevis et al., 1995; Schmid et al., 2020; Taylor et al., 1996). This triangular shape of the basin has been understood to be the result of the southward propagation of the extensional centers and their asymmetric, predominantly westward opening (Stewart et al., 2022).

While the southern Lau Basin is generally accepted to have formed at a single, though segmented axis, the evolution of the more complex northern Lau Basin remains unresolved (Sleeper & Martinez, 2016; Zellmer & Taylor, 2001). The northern Lau Basin's complexity stems from the presence of at least one other microplate (the Niuafo'ou microplate, Figure 1), as well as the increasing curvature of the trench to the north (Baxter et al., 2020; Bevis et al., 1995; Bird, 2003; Conder & Wiens, 2011; Eguchi, 1984; Sleeper & Martinez, 2016; Zellmer & Taylor, 2001). The progressive transition from trench to transform fault occurs along the westward curvature of the northern Tonga trench and is usually referred to as the Subduction-Transform-Edge-Propagator (STEP) (Bevis et al., 1995; Eguchi, 1984). This STEP is connected to the downward warping and vertical tearing of the subducting Pacific Plate at the northern termination of the Tonga trench (Millen & Hamburger, 1998). In the northern Lau Basin, the extensional motion between Australia and Tonga is divided upon multiple zones of active rifting and spreading that are located along the boundaries of the Niuafo'ou microplate (Sleeper & Martinez, 2016). This decentralized opening of the northern Lau Basin has given the emerging crust a mosaic-like signature with morphologically distinctive neighboring terrains.

The north-eastern boundary of the Niuafo'ou microplate is formed by an OSC (Figure 1), which consists of the northernmost segment of the FRSC (FRSC1) in the east and the southernmost segment of the southern arm of the MTJ (MTJ-S2) in the west (Sleeper & Martinez, 2016). The MTJ is typically separated into four segments: An ENE-oriented failed rift (MTJ-W), a northern rift with a broad axial valley, oriented NNE (MTJ-N), and two SN-oriented southern ridge segments (MTJ-S1/2). A wide neovolcanic zone is visible around the MTJ-N arm, which gradually shrinks southwards, where it ends in a narrow and patchy neovolcanic zone at the MTJ-S2 (Anderson et al., 2021). Similarly, the FRSC is made up by six overlapping, left-stepping ridge segments, which grow more arc distal toward the north (Sleeper et al., 2016). This study focuses on the northern FRSC, where the morphology is dominated by an axial valley with a ~15 km wide neovolcanic zone (Anderson et al., 2021; Sleeper et al., 2016). At the OSC, the FRSC1 and the MTJ-S2 display offset of ~25 km. A part of the crust that is enclosed in the OSC and is located north of the presented profile has been identified as trapped, pre-existing crust (Sleeper & Martinez, 2016). The presence of this trapped, pre-existing crust records past horizontal displacement both orthogonal and parallel to the ridge axes. Additionally, the analysis of centroid moment tensors (CMTs) has identified a northward growing strike-slip component along the FRSC, implying recent horizontal displacement parallel to the FRSC1 ridge axis (Baxter et al., 2020; Dziewonski et al., 1981; Ekström et al., 2012; Sleeper & Martinez, 2016).

A prominent NW-trending formation that consists of young volcanic structures and includes the island of the Niuafo'ou shield volcano crosses the northern Lau Basin approximately 75 km W of the MTJ-S2 and will be referred to as the Western Rift Margin (WRM). The WRM separates two geological terrains distinguishable by their seafloor morphology (Figure 1). While the seafloor east of the WRM displays multiple elongated ridges of roughly the same orientation as the WRM (NNW-trending), the seafloor relief west of the WRM appears more chaotic and is dominated by unaligned volcanism. Opening rates at the FRSC decrease southwards ranging from

28 mm/a at the northern tip of the FRSC to 8 mm/a in the south (Sleeper & Martinez, 2016). Opening rates at the MTJ range between 27 and 32 mm/a (Sleeper & Martinez, 2016).

2.2. Crustal Zonation of the Lau Basin

Because BABs are formed by rifting of the adjacent volcanic arc and subsequent transition to spreading (Karig, 1970; Molnar & Atwater, 1978), numerous spreading centers originate from an arc-proximal location and grow progressively arc-distal with continued spreading. Because of an increasing depth to slab and the resulting decoupling of the spreading center's and the volcanic arcs melt supplies, the subduction signature of the emerging crust is known to decrease with distance to the arc (Kincaid & Hall, 2003; Langmuir et al., 2006; Martinez & Taylor, 2002; Pearce et al., 1994). The gradual decrease of the subduction signature creates a geochemical zonation perpendicular to the ridge, which preserves an image of past spreading center-arc configurations (Dunn & Martinez, 2011; J. Hawkins & Taylor, 1995; Pearce et al., 1994). The hydration of the mantle through slab-derived fluids is described to have the greatest influence on the crustal zonation because it decreases the mantle solidus temperature (Kushiro et al., 1968) and thus increases the melt production, as well as the melt's silica content (Gaetani et al., 1994; Stolper & Newman, 1994).

Based on observations made along the Eastern Lau Spreading Center (ELSC) and Valu Fa Ridge (VFR) in the southern Lau Basin, it has been suggested that the decoupling of the volcanic arcs and the spreading centers melt sources occurs in a transition zone that is located over the ~180–190 km slab contour (Sleeper & Martinez, 2014). Within this transition zone, decoupling of the melt sources has been found to cause a sharp transition from a water-rich to a water-poor melting regime, which coincides with a shift in lava compositions from basaltic andesites to basalts (Dunn & Martinez, 2011; Martinez & Taylor, 2002; Sleeper & Martinez, 2016). While the resulting morphological changes and crustal zonations of the BAB have been studied extensively at the ELSC and VFR (Arai & Dunn, 2014; Dunn, 2015; Dunn & Martinez, 2011; Escrig et al., 2009; Martinez & Taylor, 2002; Sleeper & Martinez, 2014), the extensional region of the FRSC/MTJ-S2 is less well understood.

Along the FRSC1/MTJ-S2, the distance to the Tofua volcanic arc increases in a roughly linear fashion northward, disrupted only by the westward step at 16°20′, where the Niuatoputapu Lineament offsets the northern Tofua volcanic arc from its southern extension (Bonnardot et al., 2007; Sleeper et al., 2016). Arc distances range from ~25 km at the southern FRSC to ~75 km at the northern tip of the FRSC and have been shown to correlate with a northward decreasing subduction influence in sampled volcanic rocks (Escrig et al., 2012; Sleeper et al., 2016). Later morphological analyses of the seafloor along the axis of the FRSC/MTJ-S extensional zone linked increasing arc proximity, and thus the influence of water-rich melting, with a shoaling of the seabed as well as increasing relief of volcanic ridges (Sleeper et al., 2016). Sleeper et al. (2016) further conclude that due to the westward step of the Tofua volcanic arc, the eastern bounding faults of the FRSC1 are located above the 180–190 km slab contour and should therefore show a subduction input, which is in agreement with previous geochemical studies (Escrig et al., 2012; Keller et al., 2008). It has further been proposed that since the volcanic ridge, which is interpreted to define the FRSC1 axis, is bound by large faults and a deep basin, the FRSC1 is interpreted to have transitioned from a tectonic to a more magmatic extension (Sleeper et al., 2016). The high relief of the volcanic ridge and the presence of lava flows with lobate margins along the FRSC2 serve as arguments for recent magmatic activity along the FRSC1 and FRSC2 in Sleeper et al. (2016). This apparent shift in the predominant type of extension along the FRSC1 is ascribed to an ongoing distancing to the volcanic arc front (Sleeper et al., 2016). In contrast, both the deep and even seafloor morphology, as well as geochemical studies of dredge samples, suggest a weak or absent subduction influence at the MTJ-S2 (Keller et al., 2008; Sleeper et al., 2016).

3. Data

Data were acquired within the framework of the expedition SO267, which took place from December 2018 to January 2019 on the RV SONNE (Hannington et al., 2019). An active seismic survey was carried out along a 185-km-long transect, where 30 OBSs were deployed with a spacing of 5 km (Figure 1, red dots). An array of six G-Gun clusters with a total volume of 84 l was towed at 8 m depth and fired at ~190 bar with two different shooting intervals, 50 m for MCS recordings and 170 m for wide-angle seismic data recorded on the OBS. MCS data (Figure 1, red dashed line) were recorded with a 3.9-km-long streamer, which was towed behind the vessel alongside a magnetometer. Additionally, a sea gravimeter was installed in the vessel, which continuously recorded the

gravity field, and dredges were collected from prominent structural features for later geochemical analysis. Data and methods will be described in the following sections. Further details about the equipment and measurements can be found in the cruise report (Hannington et al., 2019).

3.1. Ocean Bottom Seismometer Data

The profile was shot twice, once for the refraction seismic survey and once for the subsequent MCS survey. Therefore, two shot records were cut out of the continuous data acquired by the deployed OBS. Later, processing of the standard seg-y records (Figures 2a, 2c, and 2e) comprised estimating the positions of the OBS on the seafloor and their relocalization to the corresponding position, a debias, a deconvolution and an offset dependent bandpass filtering. The debias is applied to the data in order to reduce the noise that is introduced by electrical components of the instruments and was undertaken using a standard high-pass filter with a cut-off frequency of 1 Hz and a pass frequency of 3 Hz. The debias is followed by a deconvolution with a prediction lag of 0.05 s and an operator length of 0.32 s. The offset dependent bandpass filtering was achieved by splitting the recorded section into four time and offset windows, each with different cut-off frequencies. Frequencies were chosen such that with increasing offset/recording time, filtered frequencies become progressively smaller. This is done because of frequency-dependent damping, which shifts the spectrum toward lower frequencies with increasing travel times. For this particular data set, the cut-off frequencies of the applied bandpass filter were 3, 8, 25, and 35 Hz for the first time window, 1, 7, 20, and 30 Hz for the second, 1, 7, 20, and 30 Hz for the third and 1, 3, 15, and 25 Hz for the last time window. The dense shot interval of 50 m was used to pick near offset phases as it allows for finer sampling and therefore a better determination of phase arrival times near the stations (Figures 2b, 2d, and 2f). Phase identification for the refraction and wide-angle reflection tomography was undertaken with the graphical user interface Pasteup (Fujie et al., 2008). Considered phases were (a) the direct arrival, (b) sediment refractions, (c) refracted waves from the upper crust (Pg1), (d) refracted waves from the lower crust (Pg2), (e) Moho reflection (PmP), and (f) mantle refractions (Pn) (Figure 2).

3.2. Multi-Channel Seismic Data

In addition to the refraction seismic data, coincident reflection seismic data were acquired with a 3.9-km-long streamer and a 50-m shot interval (Figure 1, red dashed line). Signal enhancement of every shot section was undertaken by bandpass filtering (6–80 Hz) and spike deconvolution, which was done using the corresponding source signature that was recorded at every shot. For further improvement of the signal-to-noise ratio and reduction of data redundancy, common midpoint stacking was applied using a bin size of 6.25 m. Finally, a Kirchhoff pre-stack depth migration of the section was applied using the *P*-wave velocity model derived from the preceding travel time tomography of the OBS data.

3.3. Sub-Bottom Profiler Data

The Atlas PARASOUND P70 system was used to acquire high resolution sub-bottom profiler data throughout most of the cruise. Two different waves, one with a frequency of ∼18–20 kHz (primary high frequency, PHF) and another with a frequency of ∼22–24 kHz wave, were used to create a so-called secondary high (about 40–42 kHz, SHF) and a secondary low frequency (SLF) of about 4 kHz, which is used for the sub-bottom profiling. The opening angle of the transducer array is 4° by 5°, which corresponds to a footprint size of about 7% of the water depth. Data processing and visualization were executed using IHS KingdomSuite ® software.

3.4. Potential Field Data

Magnetic as well as gravimetric measurements were carried out along the OBS transect. A system of two towed magnetometers, one Vector and one Overhauser, acquired the magnetic data, which were later subjected to standard processing and used for magnetic forward modeling. The standard processing of single channel Overhauser sensor data, as presented in this study, comprises the identification and elimination of faulty measurements, and the subtraction of the geomagnetic reference field using IGRF 2015 (Macmillan & Maus, 2005). The resulting data are resampled with a 1 s time step (Engels et al., 2008). The repeated measurement of the profile showed that the records are affected by a relatively low noise level, since the two records only show differences of up to
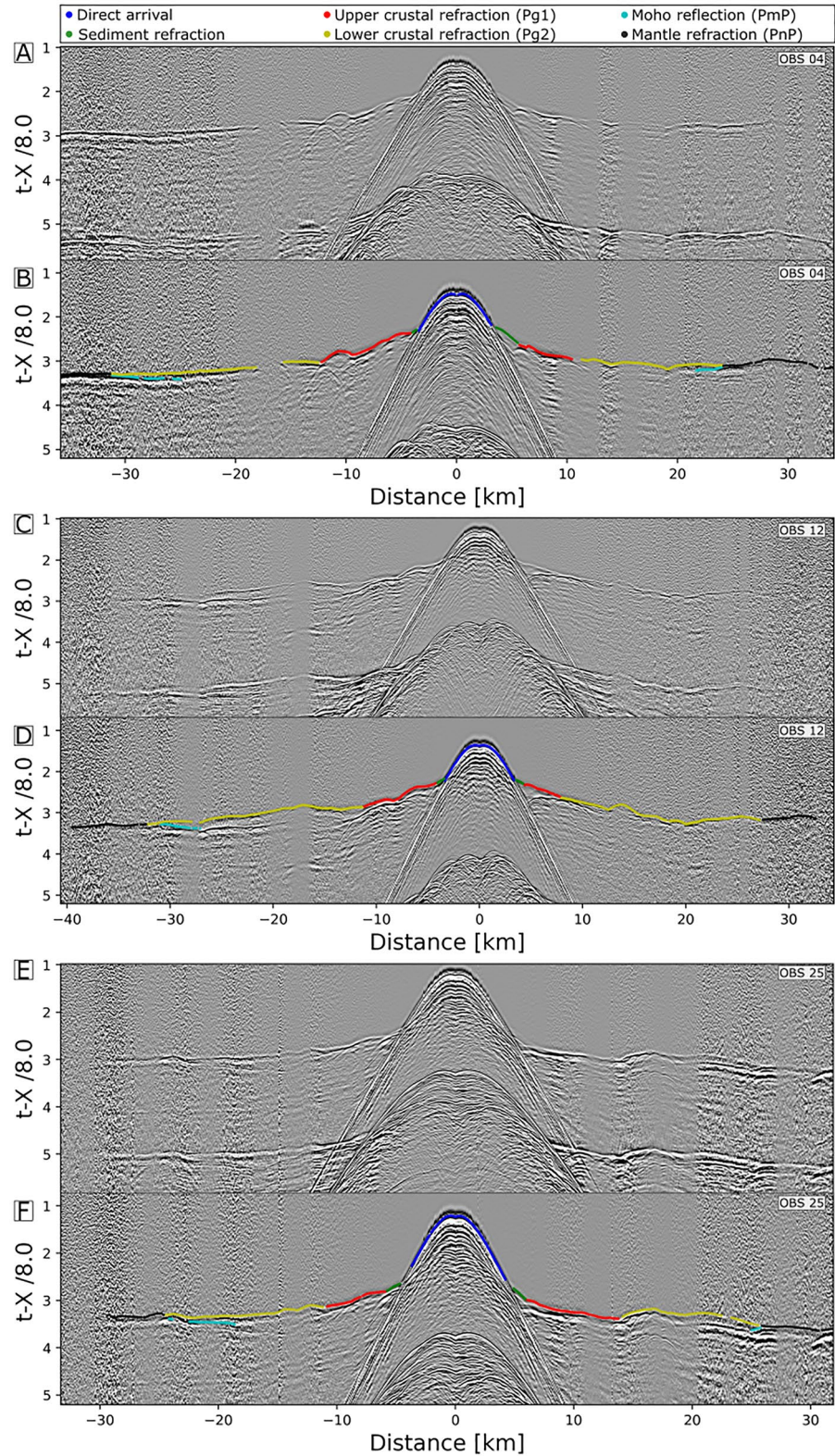
Figure 2. Exemplary seismic shot sections (OBS04, OBS12, OBS25) that were used in the seismic inversion shown without (panels a, c, e) and with superimposed travel time picks (subplot b, d, f). For visualization purposes, the processed files were chosen and visualized with a reduction velocity of 8.0 km/s despite possible filter artifacts.

30 nT, which is an order of magnitude smaller than the identified magnetic anomalies. We therefore conclude that the daily variations of the Earth's magnetic field, which cause the deviation in the repeated data measurements, were negligible during the data acquisition.

For the acquisition of the gravimetric data, a sea gravimeter KSS32-M system was installed on RV SONNE approximately 1 m above the vessel's nominal water line. The drift of the data was approximated by repeating a specific point measurement in the SUVA harbor once at the beginning and once at the end of the expedition. In order to tie the measurements to the International Gravity Standardization Net IGSN71 (Morelli, 1974) and thus guarantee their general comparability, gravimetric measurements with a LaCoste and Romberg gravity meter, model G, no. 480 (LCR G480), were executed both at the pier next to RV SONNE and at the next reference station, which was the Mineral Resources Department 01 in Suva, Fiji. These measurements were then tied to values from the database of the Bureau Gravimetrique International, Toulouse. Additional processing of the data comprised the correction of the Eötvös effect using navigation data and subtraction of normal gravity. Repeated acquisition of gravimetric data along the profile produced multiple data records, which show amplitude differences ranging between -1.15 and $+0.97$ mGal. It can therefore be concluded that the gravimetric data are of good quality.

3.5. Dredge Samples

Rock sampling on SO267 was carried out using rectangular chain bag dredges. Chain bag dredges are similar to large buckets with a chain bag attached to their bottom and steel teeth at their openings, which are dragged along the ocean floor by the ship's winch. If possible, the dredge tracks were usually located on steep slopes of scarps, canyon walls, fault zones and the flanks of cones, ridges and larger seamounts (Figure 1). In this study, the objectives of the dredging were to collect information on the geology of the seafloor and to aid the spatial and temporal reconstruction of the magmatic evolution of the arc-back-arc system by providing ground-truthing for various geophysical data. Thus, steep off-axis and intraplate structures, as well as volcanic features, were specifically targeted, complementing previous cruises that were largely constrained to spreading or rift axes (Hannington et al., 2019). In the vicinity of the profile, a total of 11 SO267 dredges recovered rocks, which were taken into consideration for the interpretation of the profile and its geological and tectonic framework (Figure 1). However, the sampled structures, as well as some key results with relevance to this study, will be briefly summarized below. Tracing the relative contributions from different mantle (e.g., depleted vs. enriched) and slab sources is mainly based on the Tb/Yb versus Nb/Yb diagram of Pearce (2008).

4. Methods

4.1. Refraction and Wide-Angle Seismic Tomography

The refraction and wide-angle reflection seismic analysis was performed based on picks of phase arrival times from records of 27 OBS. Pick uncertainties were assigned based on the appearance (e.g., clearness, focus) of their corresponding phases. On average, the upper crustal refraction (Pg1) was assigned an uncertainty of 0.03 s (Pg2), the lower crustal refraction an uncertainty of 0.05 s, the mantle refraction (Pn) an uncertainty between 0.05 and 0.07 s, dependent on the noise level, and the Moho reflection (PmP) an uncertainty of 0.07 s. The OBS records comprise arrival time data of the profile, shot twice with spacing intervals of 50 and 170 m, respectively. Forward modeling was executed in RAYINVR (Zelt, 1993) and travel time inversion was performed using the TOMO2D code (Korenaga et al., 2000). Therefore, calculations relied on a coupled graph and bending method for forward modeling and a linearized L2 norm during the inversion (Korenaga et al., 2000).

4.1.1. Forward Modeling and Sediment Thickness Approximation

Due to the limited impact of shallow sediment basins on the overall ray travel time, the MCS data were used to constrain the sediment basins and hence the basement. The derivation of the basement depth was done iteratively. A first estimate of basement depth was approximated by sampling the sediment thickness (in seconds) in regular distances along the profile and converting the seconds into a depth with an average sediment velocity of 2.25 km/s. After the incorporation of the new sediment basin/basement morphology into the initial forward velocity model, the MCS profile was depth-migrated using a Kirchhoff migration and the adapted forward velocity model. Subsequent resampling of the basement depth directly from the depth-migrated section helped to further refine the basement morphology.

4.1.2. Inversion Approach and Parameters

In order to restrict the ambiguity of the inverse problem, an adequate velocity model was determined by forward modeling of refracted phases using RAYINVR (Zelt, 1993). The phases were considered in sequence and with increasing depth, which is also referred to as layer stripping. Similarly, PmP travel times were used to find the first approximation of the Moho depth along the profile. The thus created model was then manipulated semi-randomly to create a set of new initial models for later inversion. Semi-randomness is achieved by assigning each defined model layer a deviation range, from which a random value can be selected and applied to the original model to create derivative models. Deviations for both the velocity model as well as the layer geometry were implemented.

Similar to the forward modeling, the inversion was executed in three steps: (a) inversion of all crustal phases (crustal inversion), (b) inversion of PmP and crustal phases (Moho inversion), and (c) inversion of Pn and crustal phases (mantle inversion). Three iterations were performed at each inversion step. A total of 199 models were generated for the first inversion step. Every generated model was then inverted for three iterations. The 199 final models were then averaged in order to obtain an average crustal v_p model. The resulting crustal model was then used as the basis for the second inversion step. Since the Moho was inverted as a floating reflector, the 21 semi-randomly created initial Moho geometries were merely hung into the obtained average crustal v_p model. These 21 initial models for the PmP inversion were each inverted individually with three iterations. The inversion was limited to three iterations, because all of the inverted models showed a χ^2 under 1.5 after three iterations and individual models started to overfit the travel time picks when more iterations were executed. Similar to step 1, the 21 inversion results were averaged to obtain a final Moho geometry. The combination of the final crustal model and the final Moho model was then used to create the initial models for the Pn inversion. Thirteen distinct 1D velocity profiles were hung underneath the average model obtained in step 2, in order to create 13 initial models for the Pn inversion. As in step 1 and 2, the resulting 13 final models were averaged in order to obtain a final model. This final v_p model (Figure 3a) which holds the information of all three inversion steps has a χ^2 of 0.745 and an RMS error of 0.0412 s.

As a result of the under-determined nature of the seismic inversion, constraining parameters such as the velocity-depth weighting factor (1), the velocity and depth damping (20, 30) and smoothness constraints (40, 20), as well as correlation length (horizontally: 1, 4, 10, and vertically: 0.3, 1.2, 5 for depths 0, 6, 25 km respectively) are crucial. However, the parameters' sizes are model dependent and can only be determined empirically, which was done via *L*-curve analyses.

4.2. Density Forward Modeling

First, an initial density model with a total depth of 30 km below sea level and five heterogeneous layers was inferred using the empirical v_p density relationship after Brocher (2005) and the final inverted v_p model. Thus, the created layers are similar to the seismic units: (a) the water column (1.03 kg/cm^3), (b) the sedimentary unit (2.0–2.1 kg/cm^3), (c) the upper crust (2.4–2.77 kg/cm^3), (d) the lower crust (2.9–3.0 kg/cm^3) and (e) the mantle (3.0–3.3 kg/cm^3). The geometries of the first and second layers are constrained by bathymetric data (seafloor topography) and MCS data (basement topography). The 6.0 km/s v_p isoline (Figure 3a) was used to delimit the upper and lower crusts, and the Moho reflector defined the boundary between the lower crust and the mantle. After the initial model was constructed, a subroutine GRAV2D of the Korenaga code (Korenaga et al., 2000) was used to calculate the free-air gravity anomaly model response. By manual model adaptation and subsequent calculation of the new model response, the residuum between the measured and the synthetic gravity curve was minimized, yielding a crude model of the profile's density distribution.

4.3. Magnetic Forward Modeling

The synthetic magnetic anomalies were calculated using a very simple forward model, in which a flat source layer of 0.7 km thickness and 10 A/m magnetization at 2 km depth (Layer 2A) was assumed. The source layer was created with alternating blocks of normal and reversed magnetic polarity according to the magnetic reversal timescale of Cande and Kent (1995). During forward modeling, both the spreading rate, as well as the spreading centre's location were varied. This type of forward modeling is very well matched to reproduce magnetic anomalies that are observed in oceanic crust formed by spatially and temporarily steady seafloor spreading at medium to high spreading rates. However, magnetic forward modeling is hindered when low
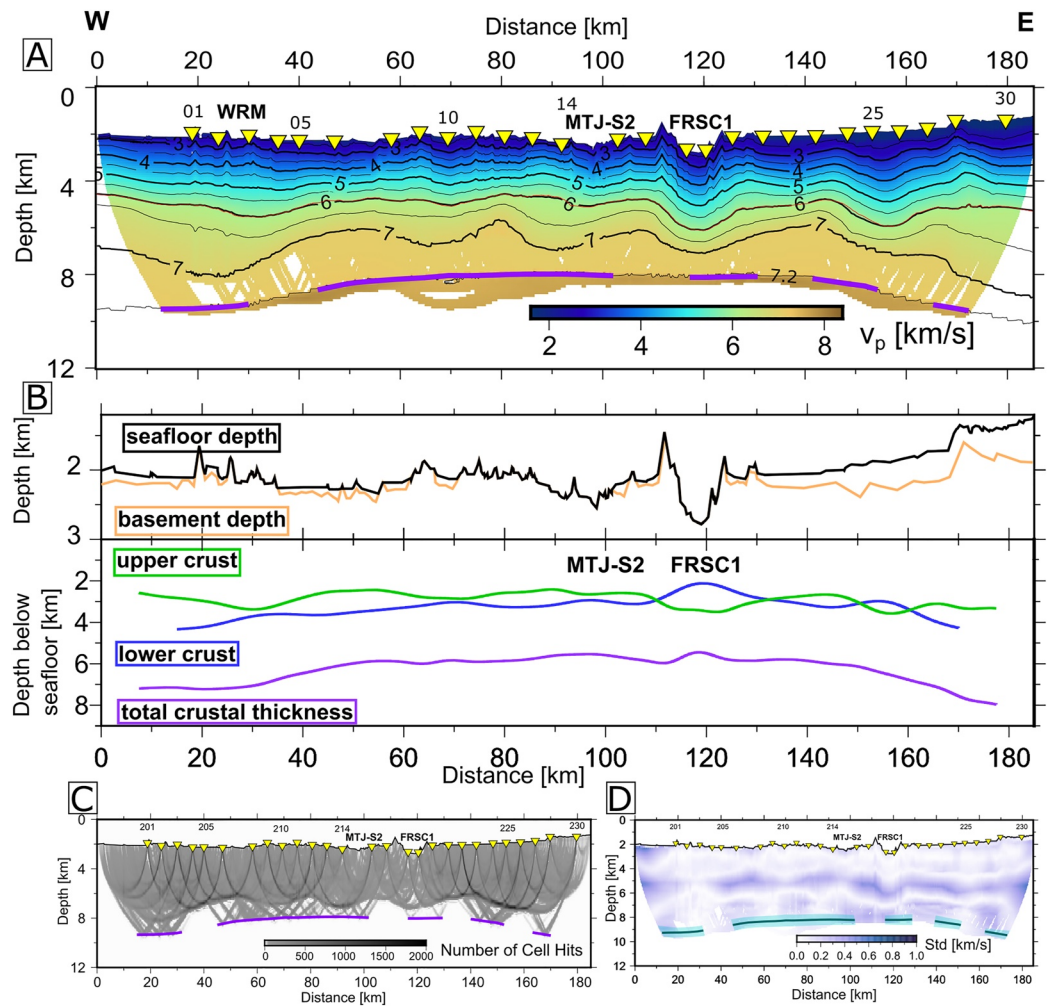
Figure 3. (a) Final *P*-wave velocity model derived from travel time inversion masked with the ray paths of the crustal phases (Pg1, Pg2) and the mantle phase (Pn). The course of the inverted Moho is marked in purple. (b) Visualization of the: basement depth (orange line), the seafloor depth (black line), the total crustal thickness (purple line), the lower crust thickness (blue line) and the upper crust thickness (green line) along the profile. (c) Density map of the calculated ray paths (Pg1, Pg2, PmP), masked with the ray paths of the crustal phases (Pg1, Pg2) and the Moho reflection (PmP). The course of the Moho (purple line) was superimposed on the density map of the calculated ray paths. (d) Model resolution shown by the standard deviation of the model and the Moho (green line) after the final iteration. The standard deviation of the velocity model is masked with the ray paths of the crustal phases (Pg1, Pg2) and the mantle phase (Pn).

spreading rates and low or discontinuous magma supply along the spreading center result in magnetic anomalies which look more diffuse than the synthetic lines. The synthetic anomalies differ from those observed in the acquired data because the basic assumptions that are made during the forward modeling, such as spatially and temporally steady seafloor spreading, or uniform crustal magnetization (apart from polarity changes), are less appropriate. However, even in complex settings such as slow spreading ridges or BAB, where processes like varying magma supply or composition, phases of pure rifting, small ridge jumps, and tectonic over-printing deform magnetic records and thus limit the possibility of magnetic forward modeling, it is usually still possible to identify distinct magnetic Chrons. Any type of extensive crustal spreading, with a magmatic component involved, will eventually create magnetic anomalies reflecting the reversals of the Earth's magnetic field and thus time marks which can be used for age dating the crust and reconstructing the local spreading history.

5. Results and Evaluation

5.1. *P*-Wave Velocity Tomography

The resulting tomography model shows a laterally smooth *P*-wave velocity distribution with an upper crustal v_p ranging between 2 and 6 km/s and a lower crustal v_p ranging between 6 and 7.2 km/s (Figure 3a). In order to visualize both the ray coverage of the Moho, as well as the degree of ray penetration into the mantle, two different masks were applied to the tomography images (Figure 3). The tomography model (Figure 3a) and the standard deviation plot (Figure 3d) are masked with the determined ray paths of the crustal phases (Pg1, Pg2) and the mantle phase (Pn). In contrast, the ray density map (Figure 3c) is masked with the ray paths of the crustal phases (Pg1, Pg2) and the Moho reflection (PmP). The Moho has been marked in locations where clear reflections can be observed. Figure 3d shows the standard deviation of the 199 v_p models after the last inversion stage. Areas with larger standard deviations represent model areas where the inversion shows less convergence, which is typically the result of low ray coverage and few crossing rays. For instance, if Figures 3c and 3d are compared, it becomes evident that the model edges show the highest standard deviations (0.6 km/s) due to unidirectional seismic illumination and thus show a greater dependence on the chosen initial model. The high standard deviation values at the boundary between the upper and the lower crusts are mostly caused by waves propagating along the bottom boundary of their respective layers, which results in reduced amounts of crossing rays. Further resolution analyses and checkerboard results can be found in Text S1 in Supporting Information S1.

The acoustic basement varies between 2 and 2.5 km depth (Figure 3b). The seismic Moho is largely flat and is located approximately 6 km under the seafloor, between 55 and 140 km profile offset. Toward both ends of the profile, the Moho deepens to nearly 8 km depth. While the described variation in the crustal thickness is mostly accommodated in the lower crust, the FRSC1 is marked by changes in both the upper (increase) and lower crustal thickness (decrease, Figure 3b). The upper crustal thickness shows many short wavelength depth variations, which appear as oscillations around an average upper thickness of about 3 km. In contrast, the lower crust shows a gradual trend of eastward and westward thickening, similar to the trend in the overall crustal thickness. The lower crustal thickness ranges from 2 km under the FRSC1 to 4 km at the eastern and western profile ends (Figure 3b).

5.2. Density Model

The profile's gravimetric data show a regional trend of eastward increasing free-air gravity anomaly values (Figure 4a), likely caused by increasing proximity to the volcanic arc. Additional masses created by the arc volcanism are compensated for in the model by gradually increasing mantle densities from 3.30 to 3.36 kg/cm³ at the base of the modeled mantle and 3.30–3.33 kg/cm³ at the top (Figure 4b).

The average lower crustal density is approximately 2.95 kg/cm³. The lower crustal density only deviates from this average value under the MTJ-S2 as well as at the very western end of the profile (Figure 4b). These lower crustal density anomalies widely coincide with density anomalies in the upper crust, where densities deviate from the average upper crustal density of ∼2.5 kg/cm³. However, many of the upper crustal anomalies are not mirrored in the lower crust, which is likely a result of the general ambiguity and decreasing resolution of gravimetric data with depth.

Positive anomalies are visible in the upper crust at the beginning of the profile from 0 to 20 km, in the larger region around the OSC (80–145 km) and lastly at ∼170 km profile offset. Negative anomalies, that stretch through the upper crust, are visible at 60–80, ∼100, ∼120 km and at 145–185 km profile offset. The later negative anomaly is pierced by the aforementioned positive anomaly at ∼170 km profile offset. Both the MTJ-S2 and the FRSC1 are visible as negative anomalies in the upper crust (∼100 and 120 km), but only the MTJ-S2 is reflected in the lower crust by an increase of densities (Figure 4b).

5.3. Magnetic Data

Because of the tectonic complexity of the northern Lau Basin, many of the basic assumptions of magnetic forward modeling, such as temporarily and spatially steady seafloor spreading, do not hold true, which is why the focus is put on the identified magnetic anomalies (Figure 4c, top) and their position along the profile rather than the magnetic forward model (Figure 4c, bottom).
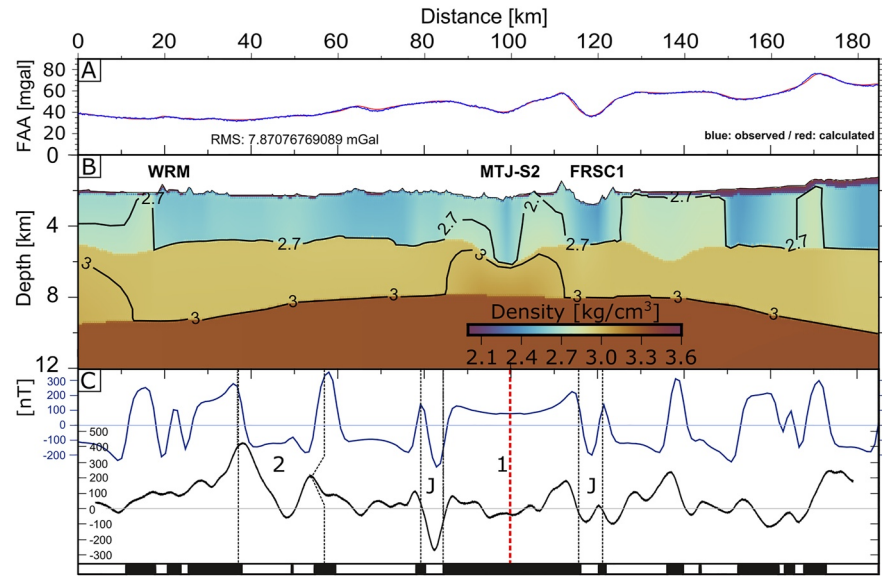
Figure 4. Observed free-air gravity anomaly data (blue line, subplot a) superimposed on the synthetic gravity model response (red line, subplot a) from the density model (b). The root mean square (RMS) of the synthetic gravity data and the acquired free-air anomaly are listed at the bottom of sublot (a). Subplot (c) displays the identified magnetic anomalies and their position along the profile. The numbers (1, 2) represent Chrons, while the J represents the Jaramillo Subchron. The black line represents the measured magnetic data and the blue line represents synthetic data from a forward model with 9 mm/a seafloor spreading. The model is shown at the bottom of subpanel (c) where the black blocks represent crust with normal magnetization and white blocks crust with reversed magnetization.

Since the amplitude of the recorded magnetic field strength depends on the distance between the magnetometer and the seafloor, strong bathymetrical variations can appear as magnetic field strength anomalies in the recorded data. Hence, in profiles with large bathymetrical variations such as the one presented, weak anomalies which coincide with sharp bathymetric features have to be treated carefully. However, the amplitudes and the wavelengths of the identified magnetic anomalies appear to correlate with magnetization contrasts in the upper crust and are thus not the result of mere bathymetrical variations (Figure 4c). Four magnetic anomalies could be identified along the profile: a Chron 1 anomaly located on the MTJ-S2, a Jaramillo anomaly located on the FRSC1, a Jaramillo anomaly west of the OSC and finally a Chron 2 anomaly near the western end of the profile (Figure 4c). While the presence of the Chron 1 can be determined clearly, any older magnetic anomalies that were identified show larger deviations from the reference model and thus appear deformed (Figure 4c). Such a deformation of magnetic anomalies could be the result of processes such as tectonic or magmatic overprinting. Because of the absence of a Chron 1 anomaly at the FRSC1, ongoing extension cannot be accommodated by spreading or be accompanied by volumetrically extensive magmatic activity. In contrast, the Chron 1 anomaly at the MTJ-S2 must be formed either by the symmetric emplacement of a considerable amount of volcanic intrusions or seafloor spreading. Thus, the manner of extension at the MTJ is dominated by magmatic activity and is either spreading or rifting with a large magmatic budget.

5.4. MCS and Sub-Bottom Profiler Data

The MCS profile shows a considerable sediment mass (Figure 5A), which suggests a relatively high sedimentation rate (Figure 5A). This high sediment influx is likely related to the volcanic arc, implying that the sedimentary units probably contain high proportions of volcaniclastic material. The thick sediment package east of the FRSC1 is likely due to high sediment influx from the volcanic arc (Anderson et al., 2021). While the sedimentary unit west of the FRSC1 is characterized by isolated and shallow but sedimented basins (<0.6 km depth), the sediment cover appears as a thick, coherent deposit (<1.1 km) east of the FRSC1. The sub-bottom profiler data confirmed that the thick, arc-proximate sediments are deposited as multiple generations of sediment waves (Figures 5D-2) (Pope et al., 2018).
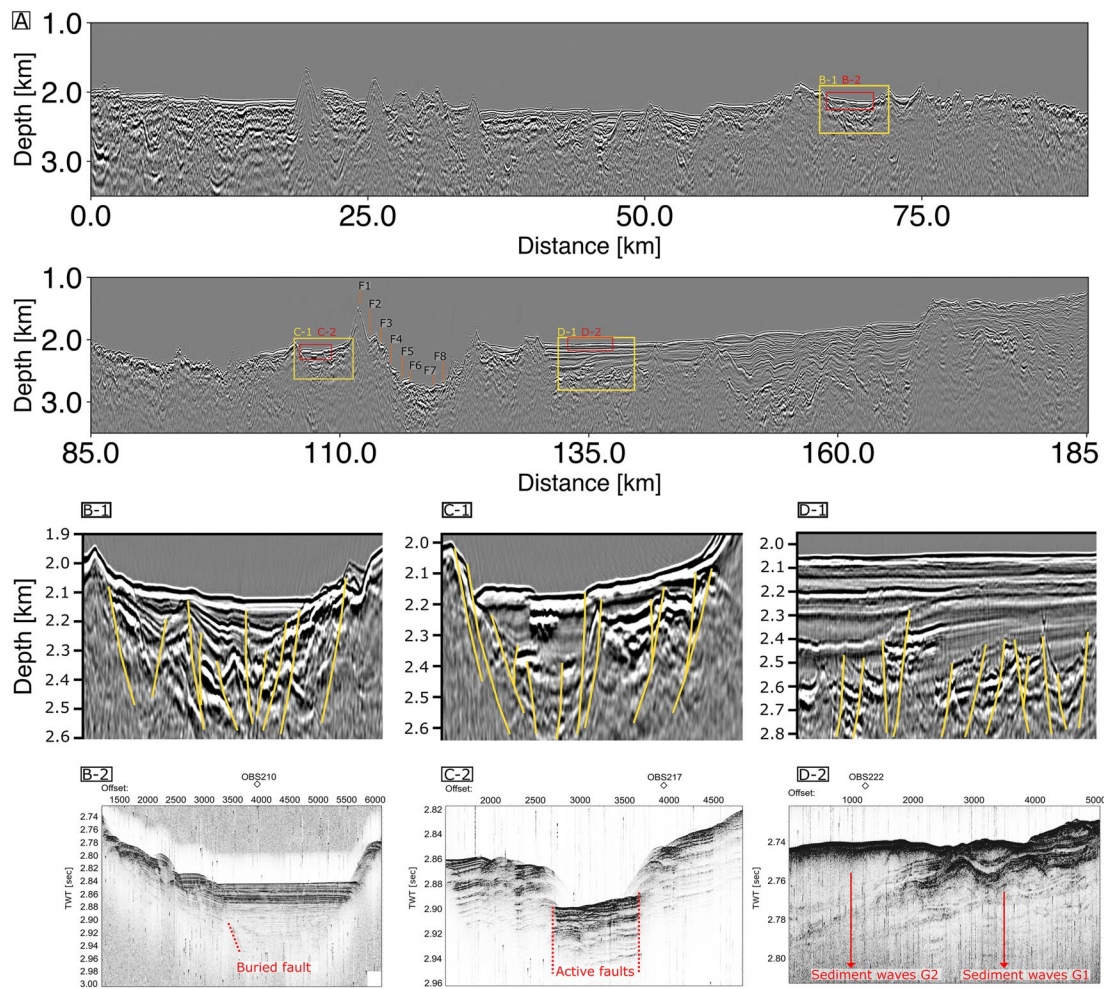
Figure 5. (A) Pre-stack depth migrated multi-channel seismic (MCS) section. The most prominent faults of the FRSC1 are marked in orange. (B1–D1) Excerpts of selected sedimentary basins of the MCS profile (yellow rectangles). (B2–D2) Sub-bottom profiler excerpts. Basement faults that are visible in the MCS excerpts of the selected sedimentary basins are marked in yellow. Similarly, prominent features of the three selected sub-bottom profiler data excerpts, presented with an automatic gain control (AGC) over a 100 ms time window, are marked in red.

Structural features along the profile include normal faults that cross-cut the basement and shape-tilted blocks, horsts and grabens, which dominate the top of the basement throughout the profile. These structural features preserve a record of past widespread extension. The grabens grow larger and deeper with proximity to the arc, indicating that the degree of extensional deformation, integrated over time, is larger close to the arc. The dipping fault geometry of the basement faults points to a normal fault activity in the past (Figure 5). However, the increasingly (semi-) vertical orientation of the faults between 120 and 135 km, compared to those further away from the OSC, points to a growing strike-slip component (Figures 5B-1–5D-1). Accumulated on top of the basement is a sedimentary unit that preceded the extension preserved in the basement, as it is strongly disturbed and follows the course of the basement. This unit marks a past extensional phase and is partly blanketed by a high impedance horizon. Since the occurrence of this high impedance horizon seems to correlate with the presence of volcanoes and grows more abundant with arc proximity, the horizon is suggested to be either volcaniclastic or effusive volcanic material. On top of this high impedance unit is a largely flat sedimentary unit that fills the grabens while not following the course of the disturbed basement and is therefore interpreted to be younger than the underlying basement deformation (Figure 5A).

Despite the abundance of visible faults, recent activity could only be confirmed for the sediment basin between the MTJ-S2 and the FRSC1 at about 110 km (Figure 5A). Here, faults actively offset the uppermost sediment layers, as is visible in the sub-bottom profiler data (Figures 5C-2). In contrast, the sub-bottom profiler data of all other
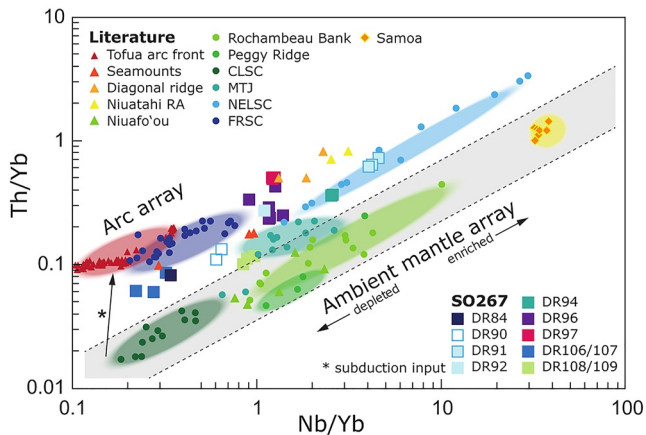
Figure 6. Plot of Th/Yb versus Nb/Yb (after Pearce, 2008) of selected data sets from the northern Lau Basin–Tofua Arc area. The diagram illustrates the competing effects of a variably enriched mantle source (or variable degree of partial melting) reflected in Nb/Yb and variable subduction input (reflected in Th/Yb). Data sources are as follows: Tofua volcanic arc front (Beier et al., 2017); North-East Lau Spreading Center (NELSC), Seamounts at the NELSC propagator, Niuatahi Rear-Arc (RA) volcano, and the Diagonal Ridge (Haase et al., 2022); Peggy Ridge, Rochambeau Bank and rifts, Niuafo'ou intraplate, and the Mangatolu Triple Junction (MTJ) (Tian et al., 2011); Fonualei Rift and Spreading Center (FRSC) (Caulfield et al., 2012; Escrig et al., 2012; Keller et al., 2008); Samoa (Workman et al., 2004).

sedimentary basins show that the identified faults are covered by a considerable amount of undisturbed sediment (e.g., Figures 5B-2). The largely non-sedimented area between 90 and 130 km profile offset, that hosts both the MTJ-S2 and the FRSC1, shows a rugged basement with a high impedance contrast, which suggests that the crust is young and igneous. In this area between 90 and 130 km profile offset, the activity cannot be analyzed with sub-bottom profiler data and thus the extent of the active deformation cannot be determined conclusively. However, given the region's apparently considerable sedimentation rate, the non-sedimented state suggests tectonic or magmatic activity that does not allow the deposition of sediment layers.

Another striking feature is the wide-spread volcanism that is found all along the profile and coincides with volcanic chains that are crossed by the profile and are visible in the bathymetry. The volcanic features show variable ruggedness, meaning that some structures have been subjected to more erosion than others and are thus likely older. For the purpose of this study, volcanic features are clustered into two groups: an older more eroded and sedimented generation (e.g., at profile kilometers 20–40, 130, 140, 170 km) and a younger generation of more rugged features (e.g., 70–100, 115, 120 km).

5.5. Geochemical Data

Dredge DR84 targeted the WRM and recovered basaltic andesites and volcaniclastic rocks. Dredges DR90 and DR91 sampled the scarps of a series of stepping normal faults at the propagating rift tip of the North-East Lau Spreading Center (NELSC) and both sites recovered basaltic andesites and volcaniclastic rocks. Basalts were recovered at dredges DR92 and DR97, which sampled two volcanic ridges within the MTJ-FRSC OSC and just north of it (Figure 1b). Further south in the OSC, at the western wall of the FRSC1's axial valley, dredge DR96 recovered basalts and altered volcaniclastic rocks from a normal fault scarp near OBS18. Dredge DR94 sampled the western arm of the MTJ and recovered basaltic andesites. Dredges DR106 to DR109 targeted potential intraplate volcanism on the Niuafo'ou microplate. Dredges DR106 and DR107 were located on the WRM and recovered basalts, basaltic andesites and altered volcaniclastics, whereas sites DR108 and DR109, which were located west of the WRM on isolated volcanic edifices in the center of the microplate, recovered basalts and volcaniclastics.

The ambient mantle array of the northern Lau Basin is understood to be represented by the N-MORB (normal mid-ocean ridge basalt) like Central Lau Spreading Center (CLSC) and the E-MORB (enriched mid-ocean ridge basalt) like Peggy Ridge (PR) and Rochambeau Bank and Rifts (RR). Hence, these systems are interpreted as an endmember group (Figure 6), which is not or least influenced by input from the subducting slab or crustal interaction. The modern Tofua volcanic arc, in contrast, represents the other endmember group (Figure 6), which shows the strongest slab addition but the most depleted mantle. All of the dredges that were collected during the SO267 expedition show some degree of subduction influence and are thus offset from the ambient mantle array. The isolated volcanic edifices that were samples in the middle of the Niuafo'ou microplate show the weakest subduction signature of all the sampled structures (Figures 1b and 6; DR108, DR109). The comparison of all the recovered samples and their location relative to the Tofua arc confirms that the degree of slab addition decreases with increasing arc offset (Figure 6).

Both the FRSC and NELSC are offset from the ambient mantle array (Figure 6). The offset away from the ambient mantel array reflects an increased slab addition, as well as a varying influx of Samoan plume material, which shifts the samples to a more Ocean Island Basalt (OIB) like, enriched mantle composition. It has to be noted, however, that Haase et al. (2022) question the presence of Samoan plume material and argue for a different OIB-like, enriched mantle component. For the purpose of this paper, we simply use data from Samoa as the enriched mantle endmember. Despite its current distance to the Tofua volcanic arc, the WRM shows a high subduction influence at the height of the presented 2D profile (Figures 1b and 6; DR84), which appears to decrease southwards (Figures 1b and 6; DR106, DR107). The volcanic ridges that were sampled in, and north of the OSC (Figures 1b and 6; DR96, DR97, DR92), suggest a mantle source that is intermediate between those of the current MTJ, FRSC, and NELSC. These volcanic ridges have previously been described as older, pre-existing
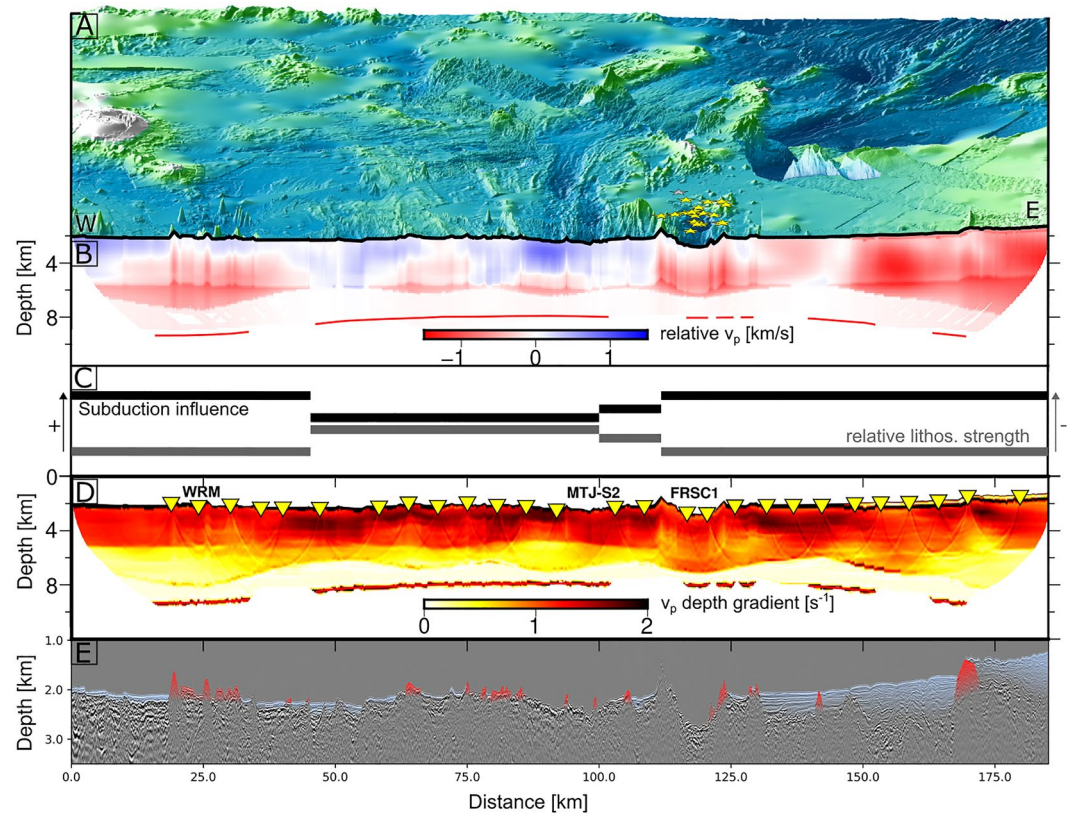
Figure 7. (a) Perspective view (20° elevation) of bathymetry data acquired during the expedition SO267, the gaps of which are filled with GMRT (Ryan et al., 2009). Cataloged earthquakes (Conder & Wiens, 2011) are marked by stars in the bathymetry if their epicenters are in the proximity of the FRSC1 or MTJ-S2. Any earthquakes with an epicenter of up to 10 km depth are marked by yellow stars, while the stars corresponding to deeper earthquakes are colored gray. (b) Relative v_p distribution calculated by the subtraction of a 1D horizontal average model (S2). (c) Qualitative illustration of the approximated subduction influence and lithospheric strength of the crust. (d) Section of the v_p depth gradient. Ocean bottom seismometer locations are marked by the yellow triangles. (e) Interpreted pre-stack depth migrated multi-channel seismic (MCS) data section exaggerated vertically by a factor 3. Volcanic features are marked in red in the MCS data section, while sedimented basins are marked in pale blue.

crust (Sleeper et al., 2016), which could explain their increased subduction input relative to the clusters of the FRSC and the MTJ (Figure 6).

5.6. Derivatives of the Velocity Model

In order to make variations in the v_p depth profile more apparent, a relative v_p distribution model was calculated (Figure 7b). This is done by calculating and subtracting a 1D average reference model from the final inversion result. This 1D average model is calculated using a routine from the tomo2D software package (Korenaga et al., 2000), which sets the velocities of the model to the corresponding horizontal average. Both the calculation of the horizontal average, as well as the later subtraction of the 1D average model are performed using the relative depth below the seafloor in order to compensate for the bathymetrical changes along the profile, the effect of which would otherwise dominate the relative v_p section. Since the 1D horizontal average model is hung directly under the seafloor, and the depth of the basement ranges from 0 to about 600 m below the seafloor (Figure 3b), the local sediment thickness influences the uppermost relative v_p of the upper crust, where the v_p depth gradient is the largest (Figure 7d). However, with increasing depth, the influence of the sediment thickness simplification decreases, since a false estimation of the sediment thickness by about 250 m would only lead to a relative v_p anomaly of 0.25 km/s in the lower upper crust and lower crust. Further details, as well as the subtracted 1D horizontal average v_p model can be found in Text S2 in Supporting Information S1. The most striking feature of the relative v_p distribution model is the general velocity decrease starting east of the 110 km profile offset, which is only interrupted by two small, positive

anomalies at ~130 km in the upper crust and ~140 km (Figure 7b). However, the apparent lower crustal anomaly at profile offset ~140 km should be viewed critically because it coincides with an area of increased standard deviation (Figure 3d). West of the 110 km profile offset, the relative v_p distribution shows much more heterogeneity. Negative anomalies are evident at ~30, ~60, and ~90 km profile offset and positive anomalies at ~50 km and in the upper crust between 70 and 110 km profile offset. While the FRSC1 is clearly marked by decreased *P*-wave velocities throughout the entire crust, the relative v_p distribution surrounding the MTJ-S2 is more chaotic and shows increased v_p down to a depth of 6 km, below which v_p appears slightly reduced (6–8 km).

The velocity gradients were calculated, since they can be used for crust type differentiation (Dunn & Martinez, 2011). Vertical v_p gradients were calculated from the average v_p model (Figure 3a) by derivation in the *z* direction, hence positive v_p gradients describe the rate of *P*-wave velocity increase with depth (Figure 7d). The shallower part of the upper crust between 2.5 and 4 km below sea level is marked by a predominant v_p gradient of ~2 s^{-1}. A few anomalies mark areas of significantly lower v_p gradients in the shallow upper crust at 0–40, 110–125, 150–160, 180 km as well as at ~100 km though less pronounced. These anomalies can be correlated with known geological structures such as the crossed WRM at 20–40 km, the MTJ at 100 km, the FRSC1 at 110–125 km and the deep sediment basin at 150–160 and ~180 km (Figures 7d and 7e). With increasing depth, the v_p gradient decreases to 1 s^{-1}. The high v_p gradient of 1 s^{-1} is constrained to a relatively thin layer that reaches down to approximately 5 km below sea level until about 110 km profile offset, beyond which it deepens. The deep lower crust shows much less variation than the upper crust and a lower predominant gradient of about 0.5 s^{-1}.

6. Discussion

6.1. Opening Mechanism of the MTJ-S2 and the FRSC1

Exposed faults and other seafloor lineaments in the area around the OSC (Figure 1) show a predominant N-S orientation at the FRSC1 and MTJ-S2 with a minor NW-SE contribution at the MTJ-S2, likely caused by the influence of the MTJ-W (Anderson et al., 2021).

A lack of seismicity prevents the determination of any CMTs and thus of the dominant fault mechanisms at the MTJ-S2. The MTJ-S2 is magmatically active, as documented by the rugged volcanic structures visible in the MCS (Figure 5) and the Chron 1 anomaly (Figure 4c). Additionally, the decreased lower crustal v_p suggests increased temperatures in the lower crust and thus the potential presence of partial melts (Figure 7b). Since the decreased upper crustal densities under the MTJ-S2 (Figure 4b) coincide with an increased v_p (Figure 7b), the mechanism at work must be one that, unlike rigid faulting, does not influence the bulk modulus of the crust significantly, while still decreasing the density. The sum of these observations leads us to conclude that the opening mechanism at the MTJ-S2 is either spreading or rifting with a large magmatic budget.

The combined presence of an axial volcanic ridge and the bounding normal faults at the FRSC1 have been interpreted to suggest a recent transition to a more magmatic type of crustal accretion (Sleeper et al., 2016). However, this assessment of FRSC1 does not match our observations. The volcanic ridge, interpreted by Sleeper et al. (2016) as FRSC1 axis, is adjacent to what could be identified as Jaramillo anomaly at the western boundary of the FRSC1 (Figure 4c). Therefore, the crust at the western boundary of the FRSC1 is likely older than the non-sedimented bounding faults, suggesting an exactly inverse transition to a more tectonic type of extension. An additional argument made in favor of increased magmatic activity at the FRSC1 is the presence of individual lava flows with relatively high backscatter at the FRSC2 (Sleeper et al., 2016). However, the extrapolation from the FRSC2 to the FRSC1 is complicated by the presence of the MTJ-S2. The magmatic activity at the MTJ-S2 has a magma starving effect on the FRSC1 because the same melt potential is now divided between the two structures. Thus, the volcanic activity at the FRSC1 is likely lower than the volcanic activity that has been observed at the FRSC2 (Sleeper et al., 2016). A volumetrically minor magmatic activity at the FRSC1 is also consistent with the deeper valley floor of the FRSC1 compared to that of the FRSC2 (Figure 1) and the absence of a Chron 1 anomaly at the FRSC1 (Figure 4c). A possible explanation for the decreased melt supply at the FRSC1 could be that the MTJ-S2 depletes the mantle before it reaches the FRSC1 and thus increases the solidus temperature despite the increased hydration of the arc-proximal mantle. This hypothesis is in agreement with numerical modeling, which showed that the extraction of melts at a BAB spreading center reduces the magmatic budget at the bordering volcanic arc segment due to mantle depletion (Conder et al., 2002).

A recent transition to a more tectonic type of extension along the FRSC1 is also in agreement with the numerous normal faults that are visible in the MCS data (Figure 5). The faults located in the FRSC1 valley display a more vertical orientation, compared to those further off-axis, which suggests a significant strike-slip component (Figure 5B1–5D1). The presence of these faults could also explain the wide zone of decreased densities and v_p, as well as the disturbance of the ambient crust stratification, which cross-cut the entire length of the crust under the FRSC1 (Figures 4b, 7b, and 7c). Anomalies in the v_p gradient trace the faults down to the shallow lower crust (Figure 7d), though faults are likely to reach even deeper since earthquakes with hypocenters of depths up to 6 km have been observed at the FRSC1 (Conder & Wiens, 2011). An alternative explanation of the reduced densities and seismic velocities, as well as the disturbance of the ambient crust stratification, could be a heat anomaly under the FRSC1. The application of the temperature derivative for v_p (-4×10^{-4} km/s K), as estimated by Korenaga et al. (2001), suggests that a temperature anomaly of 1,000 K would be necessary to produce a v_p anomaly of just 0.4 km/s. However, the degree of strike-slip related faulting and thus the degree of trans-tensional stress that is visible in the MCS image (Figure 5) and in the seismicity of the FRSC1 (Baxter et al., 2020; Conder & Wiens, 2011) is unlikely to coincide with a heat anomaly of at least ∼1,000 K. We therefore conclude that, while the presence of a heat anomaly cannot be ruled out, most of the density and v_p reduction observed at the FRSC1 must stem from rigid deformation.

The combined analysis of the profile's data shows that the FRSC1 is currently in a more tectonic type of extension that is dominated by normal faulting with a significant strike-slip component. Additionally, since faulting is limited to the extent of the OSC (Figure 5), the predominant trans-tensional stress appears to also be focused around the OSC.

Considering the shallow earthquake clusters, which exceed the FRSC1 northwards, as well as the identified strike slip faults just north of the FRSC1, it can further be concluded that the FRSC1 is propagating northwards (Baxter et al., 2020; Zellmer & Taylor, 2001).

6.2. Reconstruction of Mantle Regimes

A systematic decrease of 1 km/s is visible in the upper crustal v_p and in the shallow lower crustal v_p from the middle of the OSC (∼110 km) to the western foot of the volcanic arc at the eastern end of the profile (Figure 7). Though shifted eastward along the profile, the reduction of the v_p coincides with an increase of the lower crustal thickness that begins gradually at ∼130 km profile offset and results in an increase of the total crustal thickness from ∼6 km to a maximum of 8 km at the foot of the volcanic arc (Figure 3b). A similar pattern of geophysical properties is visible at about 20–40 km profile offset, where the WRM is crossed (Figure 1). The crust surrounding the WRM shows a similar decrease in the crustal v_p, that is accompanied by a thickening of the total crustal thickness to about 7 km (Figures 3b and 7b). A thickening of the lower crust accommodates the observed increase of the total crustal thickness surrounding the WRM (20–40 km), as well east of the FRSC1 (Figure 3b). Since an increased hydration of the melting source is known to also increase the melt production, such variations in the lower crustal thickness could be due to varying degrees of melt production and thus hydration at the time of the crust's formation. This interpretation is also in agreement with the decreased seismic velocities, since an increased hydration of the melting source is also known to increase the melt's silica content (Davies et al., 1991; Gaetani et al., 1994; Nicholls & Ringwood, 1973; Sisson & Grove, 1993; Stolper & Newman, 1994). While an increased subduction influence and thus water-rich melt source was anticipated east of the FRSC1 (Escrig et al., 2012; Keller et al., 2008; Sleeper et al., 2016), the increased crustal thickness and decreased crustal v_p, which suggest a large subduction influence at the WRM, have not been reported yet. This similarity of the WRM and the arc-proximal crust east of the OSC is also mirrored in the geochemical composition of the features. Samples recovered from the WRM show a geochemical composition that approaches that of the volcanic arc in both degree of mantle enrichment and subduction influence (Figure 6; DR84, DR106/107). We therefore suggest that the entire length of the WRM was initially formed at greater arc proximity but was subsequently transferred to its current location at greater arc offsets by ongoing seafloor spreading (Figures 1 and 8).

The WRM is now separated from the volcanic arc by a seismically faster and thinner crust (Figures 3b and 7b). This younger stretch of crust reaches from approximately 40–110 km profile offset and shows a predominantly stable total crustal thickness of 6.5 km (Figure 3b). At its eastern end, this seismically faster and thinner crust seems to progressively transition into more arc-like crust, which displays lower v_p, but lacks the lower crustal thickening observed in the arc-like crust (110–145 km, Figure 3b). While the MTJ-S2 is definitely located in
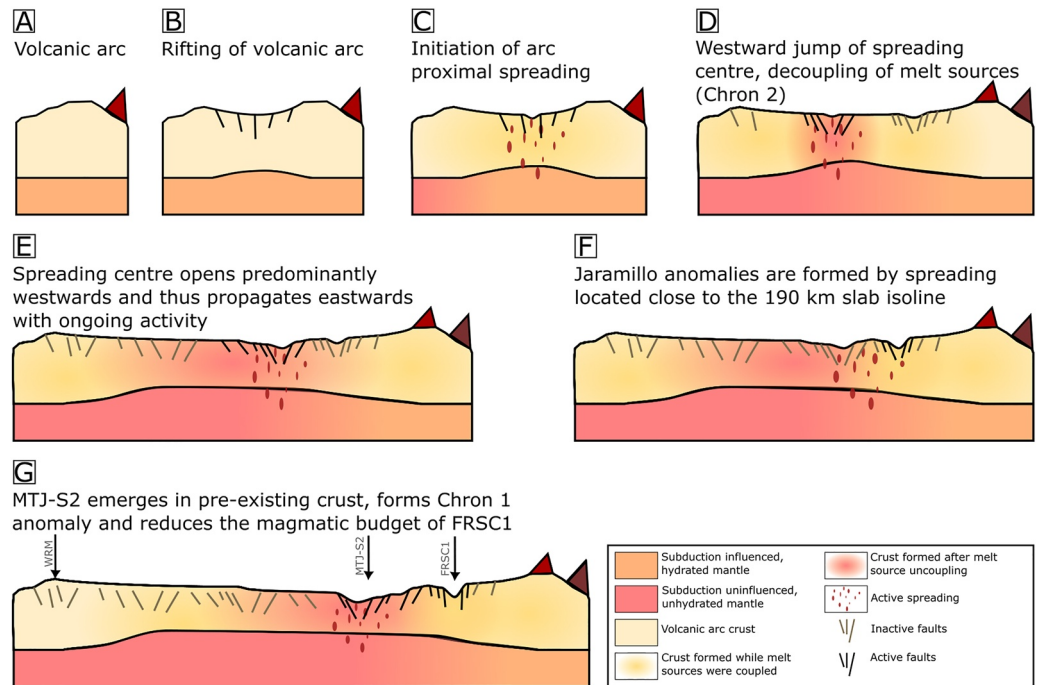
Figure 8. Schematic representation of the tectonic and magmatic evolution of the crust surrounding the overlapping MTJ-S2 and FRSC1.

this younger stretch of crust, the type of crust hosting the FRSC1 with its reduced seismic velocities, but lack of crustal thickening is less clear (Figures 3b and 7b). A compilation of geochemical data indicates significant differences in lava compositions from the MTJ-S2 and the FRSC1, which has been attributed to a more MORB-like mantle under the MTJ compared to a more arc-like mantle under the FRSC1 (Haase et al., 2022; Keller et al., 2008). The suggested segmentation of the northern Lau Basin's mantle into zones of distinct geochemical composition coincides with the presented geophysical data, as it would correlate the reduced seismic velocities with a more evolved, silica-rich crust and the stretch of seismically faster crust with a more mafic composition, which is known to show larger v_p (Behn & Kelemen, 2003). A possible explanation for the transitional character (i.e., absence of crustal thickening) of the crust close to the FRSC1 (110–145 km) could be a gradual transition between mantle regimes and their effects on the ambient crust. However, no such transitional crust can be observed at the western rift shoulder, that is, the WRM, though this could be due to the low Moho resolution between 30 and 40 km (Figure 7b). An alternate explanation for the comparatively thin crust and slow seismic velocity under the FRSC1 could also be the trans-tensional stress that is recorded in the MCS data (Figures 5C-1), which could also lead to reduced seismic velocities and crustal thinning, but would not explain the chemical differences described by Haase et al. (2022) and Keller et al. (2008), which is why we interpret the crust as transitional.

6.3. Temporal and Spatial Evolution of the Back-Arc Basin Spreading Center

The extensive magmatic activity of the MTJ-S2 is evident in both the MCS data and in the magnetic data, where it is exhibited by rugged volcanic features and a clear Chron 1 anomaly (Figures 4c and 7d). Older magnetic anomalies that were identified appear tectonically overprinted (Figure 8) and their corresponding volcanic features display weaker relief (Figure 7e). The age of the identified magnetic anomalies decreases from the WRM toward the MTJ-S2, from whereon the age appears to increase again toward the FRSC1 (Figure 4c). The oldest anomaly that could be identified is the Chron 2 anomaly that is located at the eastern boundary of the more evolved, silica-rich crust that surrounds the WRM (Figures 4c and 7b). The WRM and the surrounding crust (Figures 7b, 20–40 km) have been correlated with a more arc-like mantle source, meaning that it must have been formed in arc proximity. In contrast, two of the younger anomalies, the western Jaramillo anomaly and the Chron 1 anomaly, are located in the seismically faster and more mafic crust that separates the WRM from the volcanic

arc and has been correlated with a more MORB-like mantle with respect to its slab input (Haase et al., 2022; Keller et al., 2008). The spreading center that formed this crust must therefore have passed the 180/190 km slab isoline away from the arc during Chron 2, since its corresponding magnetic anomaly is located in the crust that was formed around the transition between an arc-like and a MORB-like melt source (Figure 8d). This transition to the arc distal side of the 180/190 km slab isoline must have occurred shortly after the initiation of spreading, since only a short stretch of the strongly subduction-influenced crust is visible at the western end of the profile (Figure 7). The asymmetric character of the magnetic anomalies along the profile, for example, the absence of a Chron 2 anomaly at the eastern end of the profile, as well as the position of the spreading center within its sub-basin suggests that the original spreading center opened predominantly westwards at the beginning of its activity (Figures 4 and 8e). Therefore, the westward movement of the spreading center during Chron 2 cannot be explained by translation as a result of ongoing spreading activity, but should be the result of processes such as ridge jumps.

If the crust between the FRSC and ~145 km profile offset is understood as transitional between crust influenced by a MORB-like mantle and crust influenced by an arc-like mantle source, the spreading center must have propagated back toward the 180/190 km slab isoline during the Jaramillo Subchron, in order to form the western Jaramillo anomaly in the crust influenced by a MORB-like mantle and the eastern Jaramillo anomaly in transitional crust (Figures 4c, 7b, and 8f). This eastward propagation is the result of the asymmetric opening of the spreading center. Either way, the spreading center must have been located on the arc distal side of the 180/190 km isoline during Chron 1, in order to form a Chron 1 anomaly in crust with little to no subduction signature (Figure 8g). Because the older magnetic anomalies show clear signs of tectonic overprinting (Figure 4c), even though the analysis of the sub-bottom profiler data conveyed that any recent tectonic activity was confined to the OSC (Figure 5), the overprinting of the magnetic anomalies W of the OSC (Figure 8f) cannot be recent. Hence, the tectonic overprinting of the Chron 2 and Jaramillo anomalies west of the present location of the OSC, as well as the Jaramillo anomaly at the FRSC1 (Figure 4c), is possibly older than the identified Chron 1 anomaly. Additionally, significant changes in the stress field must have occurred in order to focus on any ongoing rigid deformation to the extent of the OSC (Figure 5). This focusing must have occurred after the tectonic overprinting of the older magnetic anomalies and could coincide with the formation of the OSC itself. Because the identified Jaramillo Subchron anomalies are the youngest of the tectonically overprinted magnetic anomalies, the reorganization of the stress field, and thus possibly the OSC formation, can be given a maximum age of 1.07–0.99 Ma at ~16°S (age after Cande & Kent, 1995).

This interpretation would suggest that either the northward propagation of the FRSC or the southward propagation of the MTJ formed the OSC and initiated the transition to the present-day status of the FRSC-MTJ system, both in regard of extent and opening mechanism. However, because the southward propagation of the MTJ could explain the westward movement of the spreading activity that occurred between the Jaramillo Subchron and Chron 1 without another ridge jump, we believe it to be the more likely explanation.

6.4. Contextualizing the Reconstructed Spreading History

An extrapolation of this study's results, based on the morphology of the seafloor fabric (Figure 1), suggests that the sub-basin of the northern Lau Basin, that was formed at this asymmetric spreading center, should extend from the Niuafo'ou shield volcano in the north to the southern end of the WRM at about 17°20′S (Figure 1). This interpretation is in agreement with a tomographic study of the southern FRSC, in which a similar block of arc-like crust was found at the arc-distal end of the profile (Schmid et al., 2020) and geological mapping performed by Stewart et al., 2022. Because no other, active or fossil spreading center system, aside from the FRSC-MTJ system, is visible in the seafloor morphology of the sub-basin and because of its extent through all of the sub-basin (Figure 1), the FRSC-MTJ system is likely to have been the afore described spreading center that formed the sub-basin. However, based on observations made in the magnetic and MCS data, we argue that for most of the sub-basin's formation, the FRSC-MTJ system did not show the degree of overlap and possibly offset that it has today. For instance, the westward ridge jump that occurred along the profile during Chron 2 might have only taken place along the northern part of the MTJ-FRSC system and could thus have offset the southern MTJ and the northern FRSC.

6.5. Comparison to Previous Work

A dependence of the geophysical properties, such as v_p, on the melt source type has been noted in previous geophysical studies of the ELSC/VFR, where step-like changes in crustal properties have been correlated with slab-derived geochemical properties (Arai & Dunn, 2014; Dunn, 2015; Dunn & Martinez, 2011). They conclude that arc-proximal mantle with its high level of hydration and low-viscosity will produce a thicker, more porous and overall seismically slower crust than the less-hydrous and higher-viscosity mantle in arc-distal zones (Dunn & Martinez, 2011). The crust in the Lau Basin has been grouped into three crustal domains (Arai & Dunn, 2014; Dunn & Martinez, 2011; Martinez & Taylor, 2002; Sleeper et al., 2016). Domain I: oceanic crust that was formed early in the basin's history and is thus uninfluenced by the current spreading center configuration, Domain II: BAB crust formed close to the active arc (<50 km) and Domain III: BAB crust formed at a greater distance from the active arc, thus with little to no influence of hydrous melting (>70 km).

To date, the three domain crustal model has been applied to classify crust along or close to a spreading center axis and thus to relatively young crust (Arai & Dunn, 2014; Dunn & Martinez, 2011; Martinez & Taylor, 2002; Sleeper et al., 2016). The application of this three-domain crustal model to the presented profile is complicated because not just young or freshly formed crust is considered but also older crust that has been displaced from its point of formation by ongoing spreading. Since ongoing spreading forces crust away from the spreading center, the present-day arc offset is not a safe indicator of the crust's domain. Similarly, because of the increased age of the crust and thus the extended length of the considered spreading record, more spreading reconfigurations may have taken place. Indeed, the analysis of the spreading record (Section 6.2) illustrated the dynamic and ephemeral nature of the BAB spreading centers. Such spreading reconfigurations can entail a spreading center propagating or jumping away from its previous position or the emergence of a new spreading center in great proximity (Figures 8e–8g). Therefore, the current day location of a spreading center, in regard to the corresponding volcanic arc, cannot be used safely to extrapolate the adjacent crust's domain either. Aside from the arc offset, morphological constrains such as the water depth have been used to differentiate between domains (Sleeper et al., 2016). Even though the apparently westward increasing seafloor depth has been used as implication for Domain II to Domain III transition (Sleeper et al., 2016), a closer examination of the basement depth in the MCS data revealed that the sediment thickness decreases with growing arc distance, causing the apparent shoaling of the seafloor (Figures 3b and 7). Thus, many commonly applied connections between seafloor and crustal properties, that were established based on observations made at mid-ocean ridges (e.g., distance to spreading center, water depth and crustal age), are not strictly applicable in the BAB setting.

Nevertheless, based on the reduced relative seismic velocities and increased crustal thickness, both the WRM as well as the crust east of the FRSC1 could be understood as old Domain II type crust. The identification of the crust as Domain II type crust would coincide with the reconstructed spreading history (Section 6.3) and the arc-like geochemical signature of the crust (Figure 6). The crust underlying the FRSC1 has similarly decreased relative seismic velocities as the crust of the WRM or the crust at the foot of the volcanic arc (Figure 7). However, because it does not display a similar degree of crustal thickening (Figure 3b) and because the arrangement of the magnetic anomalies suggests that it was formed close to the 180/190 km isoline (Section 6.2), it could be seen as crust that is transitional between Domain II and Domain III. In contrast, the crust between the western boundary of the FRSC1 and the WRM, which shows overall higher relative seismic velocities and a shallower Moho, seems more similar to what was described as Domain III type crust.

6.6. Implications for Mantle Heterogeneity

The positive Bouguer anomaly and the high velocity lower crustal cumulates that have been described for Domain II at the ELSC/VFR (Arai & Dunn, 2014) are absent at the WRM and in the crust east of the FRSC1. We interpret the absence of a positive Bouguer anomaly (Hannington et al., 2019) to be related to the absence of the high velocity lower crustal cumulates. Increased lower crustal velocities have been observed in the subduction influenced the crust of the VFR, ELSC and FRSC (Arai & Dunn, 2014; Schmid et al., 2020). These high velocity anomalies in the lower crust are commonly understood as mafic cumulates, produced by the early suppression of plagioclase crystallization, relative to clinopyroxene and olivine fractionation caused by increased fluid contents of the melt (Eason & Dunn, 2015). However, a similar zone/layer of increased lower crustal velocities is not present in the Domain II type crust east of the FRSC1 segment or under the WRM. We derive that crustal cumulates were not formed in the crust underlying the presented profile as

the age of the crust (<5 Ma) makes significant changes in the geothermal gradient or lithostatic pressure, or the loss of such cumulates due to metamorphic overprinting or delamination unlikely. This suggests that the crust of one domain shows more variability than has been described so far. A strong geochemical variability, marked by the presence of a higher proportion of enriched, though refractory mantle in the northern Lau Basin, has been noted in previous geochemical studies (Escrig et al., 2012; Haase et al., 2022). This refractory mantle component, that is often understood to be Samoan plume material, spreads into the northern Lau Basin through the slab tear at the STEP, from where it can be traced southwards (Escrig et al., 2012; Falloon et al., 2007; Smith et al., 2001). The refractory mantle material was likely moved from under the slab and around the lateral slab edges into BAB mantle wedge by toroidal mantle return flows, which are induced by slab rollback (Schellart, 2004; Schellart & Moresi, 2013). The toroidal mantle return flows dominate the mantle flow close to lateral slab edges but lose influence with increasing distance from the lateral slab edge, where poloidal flow cells that are orientated perpendicular to the slab dominate the mantle flow (Schellart & Moresi, 2013). As the influence of the toroidal flows decreases, so does the impact of the refractory mantle source. We therefore suggest that while the different arc distances of the ELSC/VFR and FRSC-MTJ systems likely influence the intradomain heterogeneity of BAB crust, it is reinforced by a geochemically heterogeneous mantle.

A similar heterogeneity of BAB crust was described in a recent quantitative study that compares the lower crustal P-wave velocity and crustal thickness of multiple BABs (Grevemeyer et al., 2020). The authors of the study attribute the detection of both increased and decreased lower crustal velocities (relative to what was defined as normal oceanic crust) to a mantle with varying degrees of depletion, and show that this mantle heterogeneity is common in BABs around the globe (Grevemeyer et al., 2020). They further infer that in order to account for the degree of variance in the seismic properties of the BAB crust, the zonation of the BAB crust must be influenced by more than mantle hydration and thus mere arc distance (Grevemeyer et al., 2020). We suggest that the transition between toroidal and poloidal mantle flow in the BAB mantle wedge forms arc parallel mantle heterogeneity and accounts for at least parts of the variance observed.

7. Conclusions

The crust of the northern Lau Basin at ~16°S has been studied with seismic, magnetic, gravity, bathymetric and dredge sample data. We observed, that crust that is formed at the FRSC-MTJ system after decoupling from the melt source of the volcanic arc shows higher seismic velocities, a thinner crust and more mafic compositions. While these observations are in agreement with previous models of the BAB (Dunn & Martinez, 2011), they also showed that the crustal properties such as relative seismic velocities and Moho depth display more intradomain heterogeneity than the previous models describe.

We further derive that the transition from crust formed in the proximity of the Tofua volcanic arc to crust that was formed at greater arc distance is not just visible in the relative v_p, the vertical v_p gradient and the geochemistry but also influences the elastic behavior of the crust.

We could extrapolate our results in order to establish that the tectonic history of the sub-basin between 15°30 and 17°20′S is very complex and comprises a spreading center jump, an eastward propagation of the spreading center, the formation of an OSC, and the magma starving of spreading center segments. The formation of the OSC occurred after the Jaramillo Subchron and marks the beginning of the current day stress and melt supply configuration. Presently, the FRSC1 is rifting with volumetrically minor magmatic activity and is thus dominated by brittle deformation and shallow earthquake clusters, while the MTJ-S2 is predominantly aseismic, dominated by volcanic features and is actively spreading.

Above all, the reconstruction of the tectonic history has highlighted how dynamically both the position and the melt supply of BAB spreading centers change with time. Hence, spreading in BABs is not as linear a process as it is along the temporally and spatially steady mid-ocean ridges. In contrast, newly emerging or jumping spreading centers appear to form nested records of BAB spreading.

Data Availability Statement

OBS, MCS, bathymetry, and sub-bottom profiler, magnetic and gravity data are available on PANGAEA (Hannington et al., 2021, https://doi.org/10.1594/PANGAEA.945716; Jegen et al., 2022, https://doi.org/10.1594/PANGAEA.945716).

References

Anderson, M. O., Norris-Julseth, C., Rubin, K. H., Haase, K., Hannington, M. D., Baxter, A. T., & Stewart, M. S. (2021). Geologic and structural evolution of the NE Lau Basin, Tonga: Morphotectonic analysis and classification of structures using shallow seismicity. *Frontiers of Earth Science*, *9*, 665185. https://doi.org/10.3389/feart.2021.665185

Arai, R., & Dunn, R. A. (2014). Seismological study of Lau back arc crust: Mantle water, magmatic differentiation, and a compositionally zoned basin. *Earth and Planetary Science Letters*, *390*, 304–317. https://doi.org/10.1016/j.epsl.2014.01.014

Baxter, A. T., Hannington, M. D., Stewart, M. S., Emberley, J. M., Breker, K., Krätschell, A., et al. (2020). Shallow seismicity and the classification of structures in the Lau back-arc basin. *Geochemistry, Geophysics, Geosystems*, *21*(7), e2020GC008924. https://doi.org/10.1029/2020GC008924

Behn, M. D., & Kelemen, P. B. (2003). Relationship between seismic *P*-wave velocity and the composition of anhydrous igneous and meta-igneous rocks. *Geochemistry, Geophysics, Geosystems*, *4*(5), 1041. https://doi.org/10.1029/2002GC000393

Beier, C., Turner, S. P., Haase, K. M., Pearce, J. A., Münker, C., & Regelous, M. (2017). Trace element and isotope geochemistry of the northern and central Tongan islands with an emphasis on the Genesis of high Nb/Ta signatures at the northern volcanoes of Tafahi and Niuatoputapu. *Journal of Petrology*, *58*(6), 1073–1106. https://doi.org/10.1093/petrology/egx047

Bevis, M., Taylor, F. W., Schutz, B. E., Recy, J., Isacks, B. L., Helu, S., et al. (1995). Geodetic observations of very rapid convergence and back-arc extension at the Tonga arc. *Nature*, *374*(6519), 249–251. https://doi.org/10.1038/374249a0

Bird, P. (2003). An updated digital model of plate boundaries. *Geochemistry, Geophysics, Geosystems*, *4*(3), 1027. https://doi.org/10.1029/2001GC000252

Bonnardot, M.-A., Régnier, M., Ruellan, E., Christova, C., & Tric, E. (2007). Seismicity and state of stress within the overriding plate of the Tonga-Kermadec subduction zone. *Tectonics*, *26*(5), TC5017. https://doi.org/10.1029/2006TC002044

Brocher, T. M. (2005). Empirical relations between elastic wavespeeds and density in the Earth's crust. *Bulletin of the Seismological Society of America*, *95*(6), 2081–2092. https://doi.org/10.1785/0120050077

Cande, S. C., & Kent, D. V. (1995). Revised calibration of the geomagnetic polarity timescale for the Late Cretaceous and Cenozoic. *Journal of Geophysical Research*, *100*(B4), 6093–6095. https://doi.org/10.1029/94JB03098

Caulfield, J., Turner, S., Arculus, R., Dale, C., Jenner, F., Pearce, J., et al. (2012). Mantle flow, volatiles, slab-surface temperatures and melting dynamics in the north Tonga arc–Lau back-arc basin. *Journal of Geophysical Research*, *117*(B11), B11209. https://doi.org/10.1029/2012JB009526

Chase, C. G. (1978). Extension behind island arcs and motions relative to hot spots. *Journal of Geophysical Research*, *83*(B11), 5385–5387. https://doi.org/10.1029/JB083iB11p05385

Conder, J. A., & Wiens, D. A. (2011). Shallow seismicity and tectonics of the central and northern Lau Basin. *Earth and Planetary Science Letters*, *304*(3), 538–546. https://doi.org/10.1016/j.epsl.2011.02.032

Conder, J. A., Wiens, D. A., & Morris, J. (2002). On the decompression melting structure at volcanic arcs and back-arc spreading centers. *Geophysical Research Letters*, *29*(15), 17-1–17-4. https://doi.org/10.1029/2002GL015390

Davies, J. H., Bickle, M. J., Tarney, J., Pickering, K. T., Knipe, R. J., & Dewey, J. F. (1991). A physical model for the volume and composition of melt produced by hydrous fluxing above subduction zones. *Philosophical Transactions of the Royal Society of London Series A: Physical and Engineering Sciences*, *335*(1638), 355–364. https://doi.org/10.1098/rsta.1991.0051

Dunn, R. A. (2015). Tracking stress and hydrothermal activity along the Eastern Lau Spreading Center using seismic anisotropy. *Earth and Planetary Science Letters*, *410*, 105–116. https://doi.org/10.1016/j.epsl.2014.11.027

Dunn, R. A., & Martinez, F. (2011). Contrasting crustal production and rapid mantle transitions beneath back-arc ridges. *Nature*, *469*(7329), 198–202. https://doi.org/10.1038/nature09690

Dziewonski, A. M., Chou, T. A., & Woodhouse, J. H. (1981). Determination of earthquake source parameters from waveform data for studies of global and regional seismicity. *Journal of Geophysical Research*, *86*(B4), 2852. https://doi.org/10.1029/JB086iB04p02825

Eason, D. E., & Dunn, R. A. (2015). Petrogenesis and structure of oceanic crust in the Lau back-arc basin. *Earth and Planetary Science Letters*, *429*, 128–138. https://doi.org/10.1016/j.epsl.2015.07.065

Eguchi, T. (1984). Seismotectonics of the Fiji Plateau and Lau basin. *Tectonophysics*, *102*(1), 17–32. https://doi.org/10.1016/0040-1951(84)90006-4

Ekström, G., Nettles, M., & Dziewoński, A. M. (2012). The global CMT project 2004–2010: Centroid-moment tensors for 13,017 earthquakes. *Physics of the Earth and Planetary Interiors*, *200–201*, 1–9. https://doi.org/10.1016/j.pepi.2012.04.002

Engels, M., Barckhausen, U., & Gee, J. S. (2008). A new towed marine vector magnetometer: Methods and results from a central Pacific cruise. *Geophysical Journal International*, *172*(1), 115–129. https://doi.org/10.1111/j.1365-246X.2007.03601.x

Escrig, S., Bézos, A., Goldstein, S. L., Langmuir, C. H., & Michael, P. J. (2009). Mantle source variations beneath the Eastern Lau Spreading Center and the nature of subduction components in the Lau basin–Tonga arc system. *Geochemistry, Geophysics, Geosystems*, *10*(4), Q04014. https://doi.org/10.1029/2008GC002281

Escrig, S., Bézos, A., Langmuir, C. H., Michael, P. J., & Arculus, R. (2012). Characterizing the effect of mantle source, subduction input and melting in the Fonualei Spreading Center, Lau Basin: Constraints on the origin of the boninitic signature of the back-arc lavas. *Geochemistry, Geophysics, Geosystems*, *13*(10), Q10008. https://doi.org/10.1029/2012GC004130

Falloon, T. J., Danyushevsky, L. V., Crawford, T. J., Maas, R., Woodhead, J. D., Eggins, S. M., et al. (2007). Multiple mantle plume components involved in the petrogenesis of subduction-related lavas from the northern termination of the Tonga Arc and northern Lau Basin: Evidence from the geochemistry of arc and backarc submarine volcanics. *Geochemistry, Geophysics, Geosystems*, *8*(9), Q09003. https://doi.org/10.1029/2007GC001619

Fujie, G., Kasahara, J., Murase, K., Mochizuki, K., & Kaneda, Y. (2008). Interactive analysis tools for the wide-angle seismic data for crustal structure study (technical report). *Exploration Geophysics*, *39*(1), 26–33. https://doi.org/10.1071/EG08006

Gaetani, G., Grove, T., & Bryan, W. (1994). 32. Experimental phase relations of basaltic andesite from hole 839B under hydrous and anhydrous conditions (Vol. *1*, p. 135). https://doi.org/10.2973/odp.proc.sr.135.133.1994

Grevemeyer, I., Kodaira, S., Fujie, G., & Takahashi, N. (2020). Structure of oceanic crust in back-arc basins modulated by mantle source heterogeneity. *Geology*, *49*(4), 468–472. https://doi.org/10.1130/G48407.1

Haase, K. M., Schoenhofen, M. V., Storch, B., Beier, C., Regelous, M., Rubin, K., & Brandl, P. A. (2022). Effects of the hydrous domain in the Mantle wedge on Magma formation and mixing at the Northeast Lau spreading center, SW Pacific. *Geochemistry, Geophysics, Geosystems*, *23*(3), e2021GC010066. https://doi.org/10.1029/2021GC010066

Hannington, M. D., Koop, H., Augustin, N., Klauke, I., & Wölfl, A. C. (2021). Multibeam bathymetry raw data (Kongsberg EM 122 entire dataset) of RV SONNE during cruise SO267. PANGAEA. https://doi.org/10.1594/PANGAEA.929706

Hannington, M. D., Kopp, H., & Schnabel, M. (2019). RV SONNE Fahrtbericht/Cruise Report SO267: ARCHIMEDES I: Arc rifting, metallogeny and microplate evolution—An integrated geodynamic, magmatic and hydrothermal study of the Fonualei rift system, NE Lau Basin, Suva (Fiji)—Suva (Fiji), 11.12.2018–26.01.2019 [Berichte]. https://doi.org/10.3289/GEOMAR_REP_NS_49_2019

Hawkins, J. W. (1976). Petrology and geochemistry of basaltic rocks of the Lau Basin. *Earth and Planetary Science Letters*, *28*(3), 283–297. https://doi.org/10.1016/0012-821X(76)90190-4

Hawkins, J., & Taylor, B. (1995). Backarc basins: Tectonics and magmatism (Vol. *63–138*).

Heuret, A., & Lallemand, S. (2005). Plate motions, slab dynamics and back-arc deformation. *Physics of the Earth and Planetary Interiors*, *149*(1), 31–51. https://doi.org/10.1016/j.pepi.2004.08.022

Jegen, A., Dannowski, A., & Kopp, H. (2022). Ocean bottom hydrophone sgy-files of seismic refraction and wide-angle data from profile P02 during SONNE cruise SO267. PANGAEA. https://doi.org/10.1594/PANGAEA.945716

Karig, D. E. (1970). Ridges and basins of the Tonga-Kermadec island arc system. *Journal of Geophysical Research*, *75*(2), 239–254. https://doi.org/10.1029/JB075i002p00239

Keller, N. S., Arculus, R. J., Hermann, J., & Richards, S. (2008). Submarine back-arc lava with arc signature: Fonualei Spreading Center, northeast Lau Basin, Tonga. *Journal of Geophysical Research*, *113*(B8), 1–13. https://doi.org/10.1029/2007JB005451

Kincaid, C., & Hall, P. S. (2003). Role of back arc spreading in circulation and melting at subduction zones. *Journal of Geophysical Research*, *108*(B5), 2240. https://doi.org/10.1029/2001JB001174

Korenaga, J., Holbrook, W. S., Detrick, R. S., & Kelemen, P. B. (2001). Gravity anomalies and crustal structure at the southeast Greenland margin. *Journal of Geophysical Research*, *106*(B5), 8853–8870. https://doi.org/10.1029/2000JB900416

Korenaga, J., Holbrook, W. S., Kent, G. M., Kelemen, P. B., Detrick, R. S., Larsen, H.-C., et al. (2000). Crustal structure of the southeast Greenland margin from joint refraction and reflection seismic tomography. *Journal of Geophysical Research*, *105*(B9), 21591–21614. https://doi.org/10.1029/2000JB900188

Kushiro, I., Syono, Y., & Akimoto, S. (1968). Melting of a peridotite nodule at high pressures and high water pressures. *Journal of Geophysical Research*, *73*(18), 6023–6029. https://doi.org/10.1029/JB073i018p06023

Langmuir, C., Bezos, A., Escrig, S., & Parman, S. W. (2006). Chemical systematics and hydrous melting of the mantle in bac-arc basins. In D. M. Christie, C. R. Fisher, S.-M. Lee, & S. Givens (Eds.), *AGU Geophysical Monographs* (pp. 87–146). American Geophysical Union. Retrieved from https://www.agu.org/cgi-bin/agubookstore?memb=agu&cart=74913&toc=SEGM1664313&order=&book=&topic=..GM&search=

MacDonald, K. C., Scheirer, D. S., & Carbotte, S. M. (1991). Mid-ocean ridges—Discontinuities, segments and giant cracks. *Science*, *253*(5023), 986–994. https://doi.org/10.1126/science.253.5023.986

Macmillan, S., & Maus, S. (2005). International geomagnetic reference field—The tenth generation. *Earth Planets and Space*, *57*(12), 1135–1140. https://doi.org/10.1186/BF03351896

Martinez, F., & Taylor, B. (2002). Mantle wedge control on back-arc crustal accretion. *Nature*, *416*(6879), 417–420. https://doi.org/10.1038/416417a

Millen, D. W., & Hamburger, M. W. (1998). Seismological evidence for tearing of the Pacific plate at the northern termination of the Tonga subduction zone. *Geology*, *26*(7), 659–662. https://doi.org/10.1130/0091-7613(1998)026<0659:SEFTOT>2.3.CO;2

Molnar, P., & Atwater, T. (1978). Interarc spreading and Cordilleran tectonics as alternates related to the age of subducted oceanic lithosphere. *Earth and Planetary Science Letters*, *41*(3), 330–340. https://doi.org/10.1016/0012-821X(78)90187-5

Morelli, C. (1974). The international gravity standardization net 1971 (IGSN71) (p. 194)

Nicholls, I. A., & Ringwood, A. E. (1973). Effect of water on olivine stability in tholeiites and the production of silica-saturated magmas in the island-arc environment. *The Journal of Geology*, *81*(3), 285–300. https://doi.org/10.1086/627871

Parson, L. M., Rothwell, R. G., & MacLeod, C. J. (1994). Tectonics and sedimentation in the Lau Basin (southwest Pacific). In *Proceedings of the Ocean Drilling Program, Scientific Results* (Vol. 135, pp. 9–21).

Pearce, J. A. (2008). Geochemical fingerprinting of oceanic basalts with applications to ophiolite classification and the search for Archean oceanic crust. *Lithos*, *100*(1), 14–48. https://doi.org/10.1016/j.lithos.2007.06.016

Pearce, J. A., Ernewein, M., Bloomer, S. H., Parson, L. M., Murton, B. J., & Johnson, L. E. (1994). Geochemistry of Lau Basin volcanic rocks: Influence of ridge segmentation and arc proximity. *Geological Society, London, Special Publications*, *81*(1), 53–75. https://doi.org/10.1144/GSL.SP.1994.081.01.04

Pope, E. L., Jutzeler, M., Cartigny, M. J. B., Shreeve, J., Talling, P. J., Wright, I. C., & Wysoczanski, R. J. (2018). Origin of spectacular fields of submarine sediment waves around volcanic islands. *Earth and Planetary Science Letters*, *493*, 12–24. https://doi.org/10.1016/j.epsl.2018.04.020

Ruellan, E., Delteil, J., Wright, I., & Matsumoto, T. (2003). From rifting to active spreading in the Lau Basin—Havre Trough backarc system (SW Pacific): Locking/unlocking induced by seamount chain subduction. *Geochemistry, Geophysics, Geosystems*, *4*(5), 8909. https://doi.org/10.1029/2001GC000261

Ryan, W. B. F., Carbotte, S. M., Coplan, J. O., O'Hara, S., Melkonian, A., Arko, R., et al. (2009). Global multi-resolution topography synthesis. *Geochemistry, Geophysics, Geosystems*, *10*(3), Q03014. https://doi.org/10.1029/2008GC002332

Schellart, W. P. (2004). Kinematics of subduction and subduction-induced flow in the upper mantle. *Journal of Geophysical Research*, *109*(B7), 1–9. https://doi.org/10.1029/2004JB002970

Schellart, W. P., & Moresi, L. (2013). A new driving mechanism for backarc extension and backarc shortening through slab sinking induced toroidal and poloidal mantle flow: Results from dynamic subduction models with an overriding plate. *Journal of Geophysical Research: Solid Earth*, *118*(6), 3221–3248. https://doi.org/10.1002/jgrb.50173

Schmid, F., Kopp, H., Schnabel, M., Dannowski, A., Heyde, I., Riedel, M., et al. (2020). Crustal structure of the Niuafo'ou Microplate and Fonualei Rift and spreading center in the Northeastern Lau Basin, southwestern Pacific. *Journal of Geophysical Research: Solid Earth*, *125*(6), e2019JB019184. https://doi.org/10.1029/2019JB019184

Scholz, C. H., & Campos, J. (1995). On the mechanism of seismic decoupling and back arc spreading at subduction zones. *Journal of Geophysical Research*, *100*(B11), 22103–22115. https://doi.org/10.1029/95JB01869

Sisson, T. W., & Grove, T. L. (1993). Experimental investigations of the role of H_2O in calc-alkaline differentiation and subduction zone magmatism. *Contributions to Mineralogy and Petrology*, *113*(2), 143–166. https://doi.org/10.1007/BF00283225

Sleeper, J. D., & Martinez, F. (2014). Controls on segmentation and morphology along the back-arc eastern Lau spreading center and Valu Fa Ridge. *Journal of Geophysical Research: Solid Earth*, *119*(3), 1678–1700. https://doi.org/10.1002/2013JB010545

Sleeper, J. D., & Martinez, F. (2016). Geology and kinematics of the Niuafo'ou microplate in the northern Lau Basin. *Journal of Geophysical Research: Solid Earth*, *121*(7), 4852–4875. https://doi.org/10.1002/2016JB013051

Sleeper, J. D., Martinez, F., & Arculus, R. (2016). The Fonualei Rift and Spreading Center: Effects of ultraslow spreading and arc proximity on back-arc crustal accretion. *Journal of Geophysical Research: Solid Earth*, *121*(7), 4814–4835. https://doi.org/10.1002/2016JB013050

Smith, G. P., Wiens, D. A., Fischer, K. M., Dorman, L. M., Webb, S. C., & Hildebrand, J. A. (2001). A complex pattern of mantle flow in the Lau backarc. *Science*, *292*(5517), 713–716. https://doi.org/10.1126/science.1058763

Stewart, M. S., Hannington, M. D., Emberley, J., Baxter, A. T., Krätschell, A., Petersen, S., et al. (2022). A new geological map of the Lau Basin (southwestern Pacific Ocean) reveals crustal growth processes in arc-backarc systems. *Geosphere*, *18*(2), 910–943. https://doi.org/10.1130/GES02340.1

Stolper, E., & Newman, S. (1994). The role of water in the petrogenesis of Mariana trough magmas. *Earth and Planetary Science Letters*, *121*(3), 293–325. https://doi.org/10.1016/0012-821X(94)90074-4

Taylor, B., & Karner, G. D. (1983). On the evolution of Marginal basins (paper 3R1188). *Reviews of Geophysics and Space Physics*, *21*(8), 1727. https://doi.org/10.1029/RG021i008p01727

Taylor, B., Zellmer, K., Martinez, F., & Goodliffe, A. (1996). Sea-floor spreading in the Lau back-arc basin. *Earth and Planetary Science Letters*, *144*(1), 35–40. https://doi.org/10.1016/0012-821X(96)00148-3

Tian, L., Castillo, P. R., Hilton, D. R., Hawkins, J. W., Hanan, B. B., & Pietruszka, A. J. (2011). Major and trace element and Sr-Nd isotope signatures of the northern Lau Basin lavas: Implications for the composition and dynamics of the back-arc basin mantle. *Journal of Geophysical Research*, *116*(B11), e2021GC010066. https://doi.org/10.1029/2011JB008791

Wessel, P., Smith, W. H., Scharroo, R., Luis, J., & Wobbe, F. (2013). Generic mapping tools: Improved version released. *Eos, Transactions American Geophysical Union*, *94*(45), 409–410. https://doi.org/10.1002/2013eo450001

Wiedicke, M., & Collier, J. (1993). Morphology of the Valu Fa spreading ridge in the southern Lau basin. *Journal of Geophysical Research*, *98*(B7), 11769–11782. https://doi.org/10.1029/93JB00708

Workman, R. K., Hart, S. R., Jackson, M., Regelous, M., Farley, K. A., Blusztajn, J., et al. (2004). Recycled metasomatized lithosphere as the origin of the enriched Mantle II (EM2) end-member: Evidence from the Samoan volcanic chain. *Geochemistry, Geophysics, Geosystems*, *5*(4), 1–44. https://doi.org/10.1029/2003GC000623

Zellmer, K. E., & Taylor, B. (2001). A three-plate kinematic model for Lau Basin opening. *Geochemistry, Geophysics, Geosystems*, *2*(5), GC000106. https://doi.org/10.1029/2000GC000106

Zelt (1993). Documentation for RAYINVR and related programs.